Laterally String Stable Control at Large Following Distances Using DRTK and TDCP

by

Stephen Andrew Geiger

A thesis submitted to the Graduate Faculty of
Auburn University
in partial fulfillment of the
requirements for the Degree of
Master of Science

Auburn, Alabama
August 4, 2018

Keywords: lateral string stability, autonomous convoys, steering control, path following, dynamic base real-time kinematic, time-differenced carrier phase

Approved by

David M. Bevly, Chair, Professor of Mechanical Engineering
George T. Flowers, Professor of Mechanical Engineering
John Y. Hung, Professor of Electrical and Computer Engineering

Abstract

This thesis examines the lateral string stability of vehicle convoys. String stability is a type of stability that relates specifically to interconnected systems. In the case of vehicle convoys, string stability examines how the convoy, or "string", as a whole reacts to disturbances applied to the lead vehicle. When a convoy is considered string unstable, the disturbances at the lead vehicle are propagated down the stream. This occurs even if each vehicle is locally stable. When a convoy is considered string stable, those disturbances are dampened out along the string of vehicles. The idea of string stability may be formulated as both longitudinal control and lateral control problems. A longitudinally unstable string has the possibility of a vehicle wrecking into its preceding or following vehicle. A laterally unstable string has the possibility of a vehicle running off the road or wrecking into a vehicle next to it. This thesis addresses ways to prevent string instability in a lateral sense.

A classical cascaded control strategy is presented which uses feedback of lateral position error and vehicle heading error. The measurements of lateral position error and heading error are acquired using dynamic base real-time kinematic positioning solution (DRTK) and time-differencing of the carrier phase measurement for odometry (TDCP). This methodology for generating measurements allows the vehicles in the convoy to follow at much greater distances than if a camera/radar was used for measurement generation. With this architecture, a baseline control strategy where each vehicle in the convoy follows the ultimate lead vehicle is employed. This control strategy is compared against another control strategy where each vehicle in the convoy follows the immediate lead vehicle. The control strategies are compared for multiple simulation scenarios using the industry standard vehicle simulation software, CarSim.

These scenarios examine a manually driven or an autonomously driven ultimate lead and three driving scenarios: a single lane change, a double lane change, and driving on the NCAT test track. Evaluations are made based on the lateral error along the string. The results show that the immediate lead following strategy is able to achieve lateral offsets which are nearly equal to the ultimate lead following strategy; therefore, the requirements of the convoy itself should be the deciding factor for which following strategy is employed.

Acknowledgments

"Blessed be the God and Father of our Lord Jesus Christ! According to his great mercy, he has caused us to be born again to a living hope through the resurrection of Jesus Christ from the dead, to an inheritance that is imperishable, undefiled, and unfading, kept in heaven for you, who by God's power are being guarded through faith for a salvation ready to be revealed in the last time." - 1 Peter 1:3-5

Thanks to my parents for teaching me that more important than this degree or any accomplishment in my life is a relationship with God through Jesus Christ. Also, for teaching me the importance of education. You've shown me so much love and blessed me beyond what I deserve. I love you.

Thanks to Dan Pierce for all of the help he gave me, both in time and in advice. Without his help, the quality of this thesis would be much less than it is. I would thank Grant in here, but I know he prefers a six-pack of beer so I won't. Thanks to the members of the GAVLab for keeping the graduate program lively. And thanks to -dave for all of the opportunities he has made available to me.

Table of Contents

List of Figures

List of Tables

List of Symbols and Abbreviations

a, b Distance between Front/Rear Axle and Center of Gravity (m)

$\vec{b}_k$ Relative Position Vector (m)

f_c Control Frequency/Sample rate (Hz)

f_{tdcp} TDCP Sampling Frequency (Hz)

h Time-Gap/Headway

i Reference Path Waypoints

j Vehicle Number in Convoy

k Sample Instance in Leader-Follower Scenario

l Vehicle Length (m)

m Vehicle Sprung Mass (kg)

p The Order of the Poles of the Prefilter

$\vec{r}_k$ Vehicle Odometry (m)

x, y Body-Fixed Coordinate Frame (m)

C Constant Ratio between the Steering Rack and Pinion (mm/rev)

$C_{\alpha f}, C_{\alpha r}$ Front/Rear Cornering Stiffness (kg-m/s^2)

CACC Cooperative Adaptive Cruise Control

CTG Constant Time-Gap

CG Center of Gravity

DRTK Dynamic Base Real-Time Kinematic mode

ECEF Earth-Centered, Earth-Fixed

ENU East-North-Up

I_e Engine Inertia (kg-m^2)

I_t Transmission Inertia (kg-m^2)

I_w Wheel Inertia (kg-m^2)

I_z Vehicle Yaw Inertia (kg-m^2)

IED Improvised Explosive Device

L_{des} Desired Inter-Vehicle Spacing (m)

M Slope of the Average Pitman Arm Curve

MPC Model Predictive Control(ler)

N Integer Ambiguity (cycles)

NCAT National Center for Asphalt Technology

R_c Constant Rolling Resistance Coefficient

R_g Gear Ratio

R_{surf} Road Surface Rolling Resistance Coefficient

R_v Speed Varying Rolling Resistance Coefficient

R_δ Steer Ratio

RPV Relative Position Vector

RMS Root-Mean-Square

TDCP Time-Differenced Carrier Phase

V2V Vehicle to Vehicle

V_x, V_y Longitudinal/Lateral Velocity (m/s)

X, Y Reference Path Frame

ΔY Lateral Offset in Reference Path Frame (m)

V_Y Y-Velocity in Reference Path Frame (m/s)

α_f, α_r Front/Rear Slip Angle (rad)

β Vehicle Sideslip Angle (rad)

δ Vehicle Steer Angle (rad)

θ_t Angle Tangent to Reference Path Frame (rad)

κ Poles of the Prefilter

λ Wavelength (m)

ϕ_A^s Carrier Phase from Satellite, s, to Receiver, A (cycles)

ψ Vehicle Heading/Yaw (rad)

$\dot{\psi}$ Vehicle Yaw Rate (rad/s)

ω_e Engine Speed (rad/s)

ω_t Transmission Speed (rad/s)

ω_w Wheel Speed (rad/s)

l_p, l_∞ Two Types of String Stability

Chapter 1

Introduction and Background

Autonomous vehicles have become a very popular topic over the past decade; however, the idea of self-driving vehicles didn't originate a decade ago. With the introduction of adaptive cruise control (ACC) in the 90s, vehicle manufacturers have only been increasing the amount of automation found in their vehicles. This includes features such as parking assistance, lane keeping, automatic braking, and collision avoidance. As these vehicles become more advanced, questions of efficiency and safety continue to arise. One way of increasing efficiency in autonomous driving is through the use of convoying. In convoys with short following distances, there is noticable fuel savings. Considering the magnitude of the trucking industry, every percent of fuel saved amounts to millions of dollars saved. However, having short following distances is not always desirable. For instance, in military convoys there are times when having large separation distances is optimal, since they may help reduce the amount of collateral damage in a situation where a vehicle in the convoy triggers an improvised explosive device (IED).

Since convoys are complex interconnected systems, careful consideration must be given to their stability. A type of stability which directly relates to interconnected systems is known as string stability. String stability examines how the convoy, or "string", reacts to disturbances as a whole. When a convoy is considered string unstable, the disturbances at the ultimate lead vehicle (the vehicle at the front of the convoy) are propagated down the stream. A string stable convoy attenuates disturbances along the string of vehicles. String stability may be formulated in both the longitudinal and the lateral directions.

1.1 Prior Research

Convoying has been an area of research for many years. Researchers have developed various methods of relative positioning as well as controllers for path duplication. In the area of string stability, prior work has generally addressed achieving longitudinally string stable convoys. However, in recent years, researchers have begun to examine the case of lateral string stability. Some of the most prominent results of their research are summarized in the following subsections.

1.1.1 Alternate Relative Positioning Methods

Any sensor that can return a range and azimuth angle may be used to generate a relative position. Of course, the specifications of the sensor determine the accuracy of the recorded range and angle. A RADAR is one such sensor. RADARs come standard in today's vehicles. Typical measurements of a RADAR are range, range rate, and azimuth angle. RADARs are used in ACC (relative position to immediate lead), back up warnings (relative position to objects), and lane change warnings (relative position to vehicles in alternate lane).

While it is possible to use camera or LiDAR for relative positioning, it is a much more tedious process than RADAR. Image/point processing algorithms must be applied to the raw data to assess which points are associated with the lead vehicle. This is the only processing step since point clouds return relative position to the LiDAR. However, image-based ranges require further computation. Because of the difficulty associated with determining the relative position vector (RPV), the use of camera and LiDAR for RPV determination is less common.

A common problem among RADAR, LiDAR, and cameras is that each sensor requires visibility of the immediate lead vehicle. In this work, a method developed by Travis and Martin, which exploits the precision of the GPS carrier phase measurement, is used for relative positioning [1]. Their formulation does not require the lead

vehicle to be in sight of the following vehicle; as a matter of fact, separation distance is rather arbitrary. However, it does require GPS availability.

1.1.2 Longitudinal String Stability

The roots of string stability research are in longitudinal string stability. Darbha, though not the first to consider string stability, gave great characterization to the topic and made many definitions which are still used today [2]. In his dissertation, he examined different spacing policies for convoys. He designed various decentralized control algorithms and evaluated them with regard to their ability to attenuate the maximum spacing errors between vehicles. His final result was a decentralized adaptive controller which is robust to parametric uncertainty through the use of a gradient adaptive algorithm which updates the uncertain parameters.

Liang and Peng developed a two level ACC system [3]. The two levels presented were an optimal high level controller which outputs a desired acceleration and a low level adaptive controller which incorporated the servo dynamics. The optimization was performed using a bilateral z transformation technique. Using this formulation, they were able to achieve string stability using a constant-headway following policy meaning that the time separation between two vehicles remained constant along the convoy. They validated their controllers using a simulation program, known as ACCSIM, developed at the University of Michigan.

Ploeg et al. presented a definition of string stability of nonlinear cascaded systems using input-output properties [4]. Their work assumes a homogeneous platoon, and their controller is based on the longitudinal following error along with its first and second derivatives. They define l_p string stability as an extension to l_2 and l_∞ (these definitions of string stability will be given more attention in Chapter 4). They validated their controller design using six passenger vehicles equipped with V2V communication.

Xiao and Gao considered both homogeneous and heterogeneous convoys in their control design [5]. In developing the vehicle model, they considered actuator and sensor delay. They developed a controller using sliding-mode techniques which was then realized as a PD controller with feedforward of the vehicle's acceleration information. The authors evaluated how time delays and time lags affect the string stability of a convoy. They demonstrate that not considering parasitic time delays in the string stability of a convoy will lead to impractical results.

Kianfar et al. divide the control into three subproblems [6]. First, they designed a longitudinal headway controller in the frequency domain to achieve longitudinal string stability. Next, they applied a corrective controller to the headway controller so that their time constraints were met. Finally, they used a model predictive controller (MPC) to perform lateral control. They implemented convex optimization on the corrective controller and the MPC to guarantee global optimality. This prior work shows that the longitudinal string instability problem has been handled in a variety of ways including optimal and adaptive controllers.

1.1.3 Lateral String Stability

Lateral string stability has begun to receive more attention since longitudinal string stability has been characterized. Solyom and Arash Idelchi developed a controller to guarantee l_∞ string stability [7]. They used camera and RADAR for measuring lateral error. To achieve string stability, the lateral error and steering wheel angle of the immediate lead is used as feedforward to the current vehicle (from here on known as the ego vehicle). The authors assume homogeneous vehicles since they use the preceeding vehicle's steering wheel angle directly.

Jansen examined string stability in terms of rotation rate meaning the yaw rate would be dampened along the string [8]. This formulation is fine in the event lateral position is not a significant vehicle state since lateral position may still be string

unstable. To achieve string stability in this sense, Jansen used feedforward of the immediate lead's steering wheel angle and total rotation rate. He designed his controller using state-variable analysis. He used radar and camera for relative position measurements, and validated his architecture using two Toyota Prius IIIs [9]. Hassanain improved upon Jansen's result by designing an $\mathcal{H}_\infty$ controller. Using his controller formulation, Hassanain was able to achieve string stability in terms of lateral position too. Hassanain's controller only used feedforward of the previous vehicle's total rotation rate and would therefore be able to extend to heterogeneous vehicles.

Kianfar et al. addressed lateral string stability in [10]. The MPC controller they designed for lateral control was redeveloped to consider string stability. They address string instability by applying a time-domain, inequality constraint to the controller. The constraint was such that it guaranteed that the ego vehicle's path would produce smaller lateral deviations than the maximum error between the immediate lead's optimal open-loop path and its intended path. Once again, convex optimization was used to guarantee global optimality.

McAree and Veres developed a sliding-mode controller which exhibited string stability in the presence of sensor and actuator delays [11]. The RPV was estimated using a camera system. The authors used feedforward of the immediate leads heading and lateral position. They validated their design by simulating it using The Open Race Car Simulator (TORCS). The measurement sample rate and control frequency was 50 Hz.

All of the previous work in lateral string stability assumes small separation distances since the lead vehicle remained in view; however, this is not always the case. A small separation distance limits the maneuvers a convoy is capable of because the lead vehicle must remain in view of the sensors. In a scenario where the lead vehicle turns a corner, the following vehicle will not be able to follow it accurately if the lead vehicle is out of view.

1.2 Contributions

The previous work in the area of lateral string stability is limited to line of sight following of the lead vehicle because of the use of camera and RADAR for RPV determination. It is also limited to an immediate lead following strategy because the RPV measurements are based on the vehicle directly in front of the following vehicle. Though it is the typical scenario, the previous work only considers a manually driven ultimate lead.

In this work, dynamic base real-time kinematic (DRTK) positioning is used for relative positioning between the leader and the follower, while time-differencing of the carrier phase (TDCP) measurement is used for odometry updates of the follower. This methodology allows the lead vehicle to be out of sight of the following vehicle while still achieving accurate path duplication and a laterally string stable convoy. For path following control, a classical, cascaded architecture is employed which uses feedback of lateral error and heading error with respect to the lead vehicle's path. The controller achieves string stability in a lateral position sense. Two path following architectures are compared. In the first, each vehicle follows the ultimate lead vehicle of the convoy, i.e., the front vehicle. In the other architecture, each vehicle follows its immediate lead vehicle, i.e., the vehicle directly in front of it. These architectures are compared using four dynamic scenarios: a single lane-change, a flat oval track, and a banked oval track. The contributions made to the field by this thesis are summarized below:

- Easy to follow classical, cascaded control design for lateral string stable convoy.
- Evaluation of string stability given immediate lead or ultimate lead following.
- Evaluation of string stability given a manually driven or an autonomously driven ultimate lead.

1.3 Thesis Outline

This work is organized into the following Chapters:

- Chapter 2 provides details on DRTK and TDCP as well as how the measurements of lateral offset and heading offset from the path are determined.
- Chapter 3 describes the lateral, dynamic bicycle model and the equations used in the controller development.
- Chapter 4 provides an in-depth look at how the cascaded controller was designed as well as a look at string stability criteria.
- Chapter 5 presents a detailed comparison of immediate lead versus ultimate lead following in various driving scenarios.
- Chapter 6 summarizes the work detailed in this thesis and presents some ideas for future work.

Chapter 2

Relative Positioning for Lateral Following

In leader-follower scenarios, it is desired that the following vehicle replicate the lead vehicle's trajectory as accurately as possible. As mentioned in Section 1.1.1, previous work has used cameras and RADAR to track and follow the leader. To directly calculate the follower's lateral offset and heading error from the lead vehicle's path, the measurements of the leader are delayed until the following vehicle reaches the past position of the leader where the measurements were taken. The disadvantage to this technique is that cameras and radars are limited to line of sight following. This chapter details a method of relative positioning which uses a dynamic base real-time kinematic positioning (DRTK) solution paired with time-differencing of the carrier phase (TDCP) measurement to achieve a highly precise lateral offset and heading error.

2.1 Dynamic Base Real-Time Kinematic Positioning

DRTK is based on the differential GPS formulation known as real-time kinematic (RTK) positioning. DRTK is a high precision, relative positioning method for determining the relative position of a rover in close proximity (<20 km) to a moving base station. In RTK, the GPS position of the base station is assumed to be known with high accuracy so that an accurate global position of the rover can be calculated. DRTK assumes a dynamic base station; in this case, only the relative position between the vehicles is important. Both RTK and DRTK use carrier phase measurements, instead of code phase measurements, to determine a relative position solution. While code phase measurements are unambiguous (meaning a biased and

noisy measurement of the range between the user and the satellite is known, i.e., pseudoranges), their typical accuracy is about 0.5 meters; whereas carrier phase measurements, which are ambiguous (unknown range between the user and the satellites), have a typical accuracy of about 5 mm. Since raw carrier phase measurements are ambiguous, the ambiguity is estimated in the DRTK algorithm[1].

2.2 Time-Differenced Carrier Phase Odometry

The same carrier phase measurements described in the previous section are used here. However, instead of being used to estimate a high precision RPV, they are used to estimate a high precision odometry measurement for a single receiver. The odometry measurement is a measurement of the change in position of the receiver from time t_{k-1} to time t_k. For short periods of time, multiple measurements of the carrier phase are highly correlated. Therefore, by differencing them, common error sources may be removed[2].

2.3 Feedback Measurement Derivation

Once estimates of the RPV and the odometry of the follower have been made, they are applied to a path following scenario as illustrated in Figure 2.1. The red and green vehicles represent the current time, and the gray vehicles represent past positions. At each time step, the following vehicle records its RPV to the leader, $\vec{b}_k$, and its odometry, $\Delta\vec{r}_k^f$. The distance between the current position of the follower and a past position of the leader, denoted by $\vec{b}_{k|k-n}$, may be found by subtracting the follower's odometry samples $k-n$ to k from the RPV at sample $k-n$. This idea is

[1]For further details on the RPV derivation, see Appendix A.1 or [12].
[2]For further details on the odometry measurement derivation, see Appendix A.2.

expressed mathematically below.

$$\vec{b}_{k|k-n} = \vec{b}_{k-n} - \sum_{q=k-n}^{k} \Delta\vec{r}_q^{\,f} \tag{2.1}$$

This enables the following vehicle to have a large separation distance from the lead vehicle while maintaining a small separation distance to the virtual lead.

The calculated virtual lead positions are used to build a reference path. The following vehicle retains all of the virtual lead waypoints in front of it and the waypoint it has just passed, denoted by $i-1$; all other past waypoints are stripped from the path since they are unnecessary. The $i-1$ waypoint is used to calculate the lateral offset from the reference path, ΔY, and the angle tangent to the path, θ_t, as shown in Figure 2.2. Where θ_t is calculated as

$$\theta_t = \text{atan2}\left(\frac{N_i - N_{i-1}}{E_i - E_{i-1}}\right) \tag{2.2}$$

Note that ΔY is perpendicular to the path frame and not the body-fixed frame. The yaw of the vehicle, ψ, is estimated using a planar GPS/INS navigation filter [13].

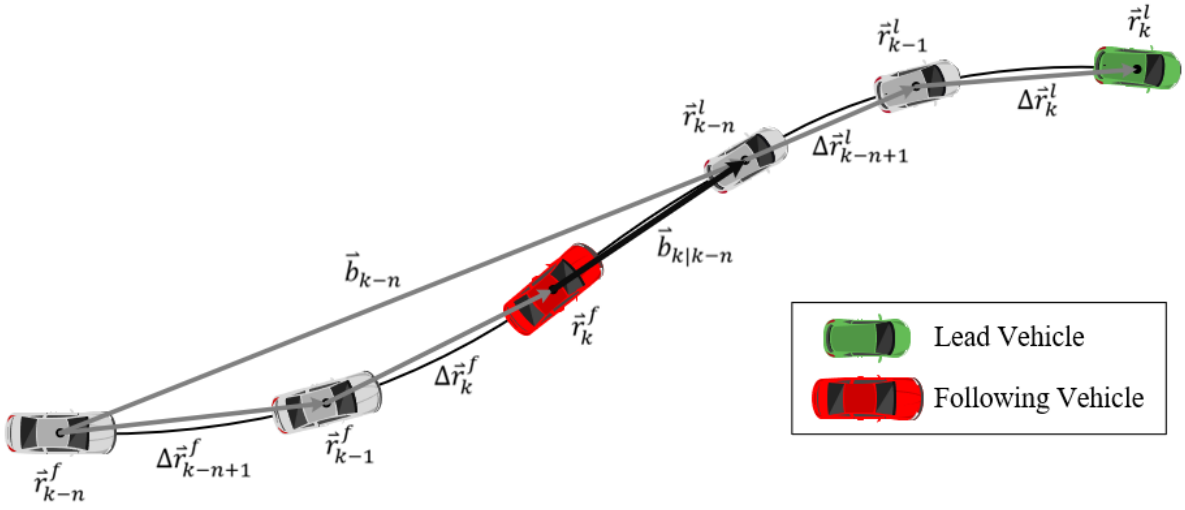

Figure 2.1: Illustration of the Leader-Follower Problem and the Available Measurements.

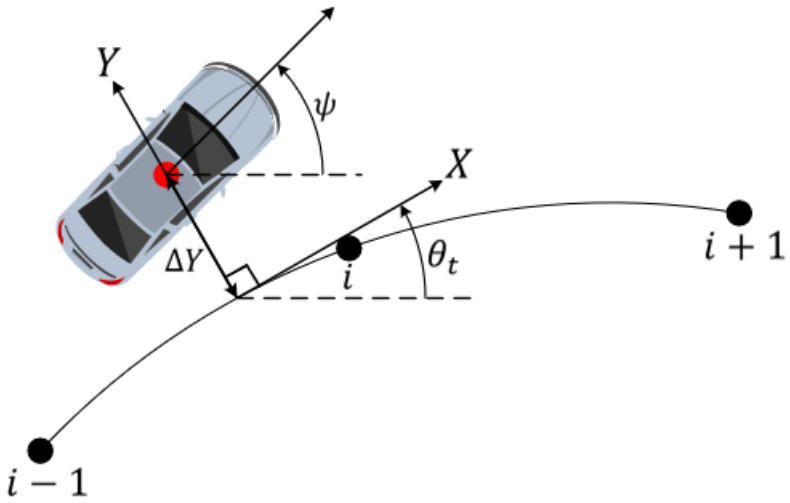

Figure 2.2: Ego vehicle's relation to the reference path.

The waypoint spacing is defined by the user. At initialization, if the vehicles already have a large separation distance, then the waypoint spacing can largely affect the initial lateral errors from the path. This is illustrated in Figure 2.3. The blue

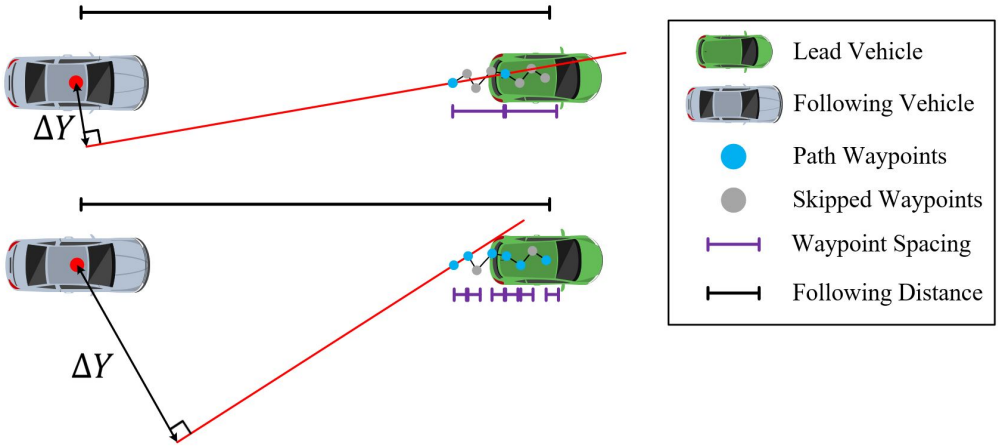

Figure 2.3: Large Waypoint Spacing (Top) vs. Small Waypoint Spacing (Bottom) at Initialization.

points are the waypoints which satisfy the minimum separation requirement and are included in the path. While the grey points are the waypoints which are not far enough away from the last path waypoints and are, therefore, rejected. As can be seen in Figure 2.3, a larger waypoint spacing reduces the error on the lateral offset measurement. However, once the following vehicle has passed the initial position of

the lead vehicle, this is no longer a problem. In most scenarios, a convoy will begin in close proximity to each other, and if a large following distance is desired, then each vehicle will depart one at a time. In this work, a minimum waypoint spacing of 0.5 m was used.

2.4 Error Limitations

Since this method of relative positioning is highly dependent on the DRTK and TDCP solutions, it is important to consider their limits in accuracy and how the accuracy will affect the convoy. Travis showed the standard deviations of DRTK and TDCP for a 20 minute and 85 minute static dataset, respectively [14]. In each case, he determined the standard deviation of the North and East errors. DRTK was applied between two antennas which had a 2 m baseline. This setup resulted in a 0.70 cm in the North direction and 0.68 cm in the East direction. TDCP was applied to a single antenna, and had standard deviations of 0.75 mm and 1.09 mm in the North and East directions, respectively. The variation in error between the North direction and the East direction is due to satellite geometry. In order to have a direction agnostic error characteristic, the root-mean-square (RMS) error was calculated for the DRTK and TDCP errors.

$$\text{RMS Error} = \sqrt{\frac{\sigma_N^2 + \sigma_E^2}{2}} \tag{2.3}$$

The RMS error for DRTK was 0.69 cm and the RMS error for TDCP was 0.94 mm.

A second characteristic of the TDCP was explored in this work: the errors of the odometry of TDCP as it relates to sampling frequency, following distance, and longitudinal velocity. The concept is illustrated in Figure 2.4. The number of TDCP measurements, n, required for the following vehicle to reach the position of the leader at the time when the RPV measurement, E_1^l, N_1^l, was calculated, is related to TDCP

sampling frequency, f_{tdcp}, following distances, L, and the following vehicle's longitudinal velocity by

$$n = \text{round}\left(\frac{L}{V_x^f} f_{tdcp}\right) \tag{2.4}$$

Static TDCP data was collected at 10 Hz using the two antennas mounted on top of the Woltosz Engineering Research Lab at Auburn University. The dataset was about 1 hour long. The dataset was downsampled to 1 Hz and 5 Hz. While this makes the assumption that the internals of the receiver do not change with sampling frequency, the results give a characterization of what the accumulated TDCP errors will be in the 1 Hz and 5 Hz sampling frequency cases. Using Equation (2.4) and the static data, every n samples were summed over along the datasets. Then the standard deviation was taken of the summed samples in the East and North directions. An RMS error was calculated from the East-North standard deviations using Equation (2.3). Velocites of 5, 10, 20, 35 m/s and following distances of 10, 50, 100, 300 m were assessed. The results are shown in Figure 2.5. Separation time is the following distance divided by the longitudinal velocity. The largest accumulated odometry RMS error is 3.2 cm in Figure 2.5, where the separation time is 1 minute and the sampling frequency is 10 Hz. The simulations in this thesis use a separation time of 14.5 seconds with a TDCP update rate of 10 Hz; therefore, the expected accumulated odometry RMS error is about 1.20 cm. This means that although the control error may be zero, the global error may be about 1.20 cm.

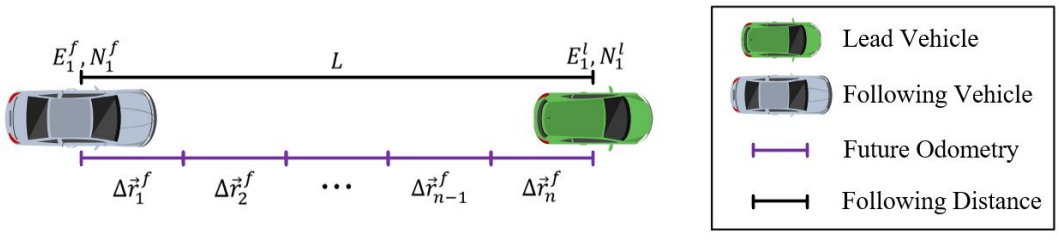

Figure 2.4: TDCP Odometry Error Accumulation Problem.

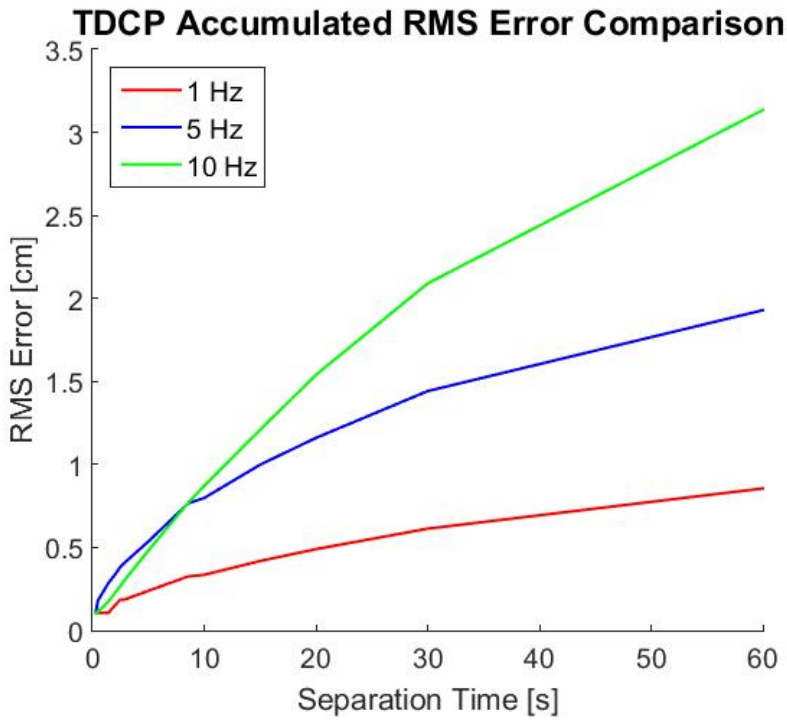

Figure 2.5: TDCP Accumulated Odometry RMS Error.

2.5 Conclusions

A method of relative positioning based on precise GPS positioning using DRTK paired with TDCP odometry was presented. The DRTK and TDCP algorithms were presented in sufficient detail for a general understanding of the algorithms; for more detailed explanations, see [1]. Using these algorithms, the measurements used for feedback in the controller design were introduced. Measurements of lateral offset and heading offset from a reference path based on the leader's previous positions were described. Initialization of the path following and how waypoint spacing affects the calculated offsets was considered.

With a general understanding of the algorithms, consideration towards the errors associated with DRTK and TDCP were made. The errors for DRTK in the East and North directions are on the centimeter level, and the errors for TDCP in the East in North directions are on the millimeter level. The accumulated TDCP RMS errors

were examined for various sampling frequencies, following distances, and longitudinal speeds. For the simulations presented in this thesis, an accumulated odometry RMS error of about 1.20 cm is expected.

Chapter 3

Vehicle Models for Controller Design

Depending on the application, differing degrees of fidelity are required in vehicle modeling. There are many scenarios where the lateral dynamics of the vehicle receive low excitation; therefore, assumptions about the dynamics can be made to simplify the model. In normal highway driving, the roll dynamics of a vehicle are typically negligable so the roll dynamics may be neglected. The yaw angle with respect to the reference path is assumed to be within the bounds of the small angle approximation, so the yaw dynamics may be linearized. These and other assumptions (which are outlined in the chapter) allow for the derivation of linearized equations of motion (EOM) that provide sufficient fidelity for controller design. This chapter details the vehicle models used for the development of the lateral and longitudinal controllers.

3.1 Lateral Bicycle Model

The vehicle model used in this work is the lateral dynamic bicycle model, shown in Figure 3.1 along with the corresponding variables. Note that the origin of the model is at the center of gravity (CG) of the vehicle. The bicycle model provides sufficient characterization of the vehicle's dynamics for the design of the controllers used in this thesis. The assumptions of this model are: equal steer and slip angles in the front left and front right tires, equal slip angles in the rear left and rear right tires, and negligible roll and pitch dynamics.

Since the work in this thesis considers highway driving scenarios, the tire dynamics are assumed to remain in the linear portion of the tire curve. Also, all angles are assumed to be within the small angle approximation, which is accurate for angles less

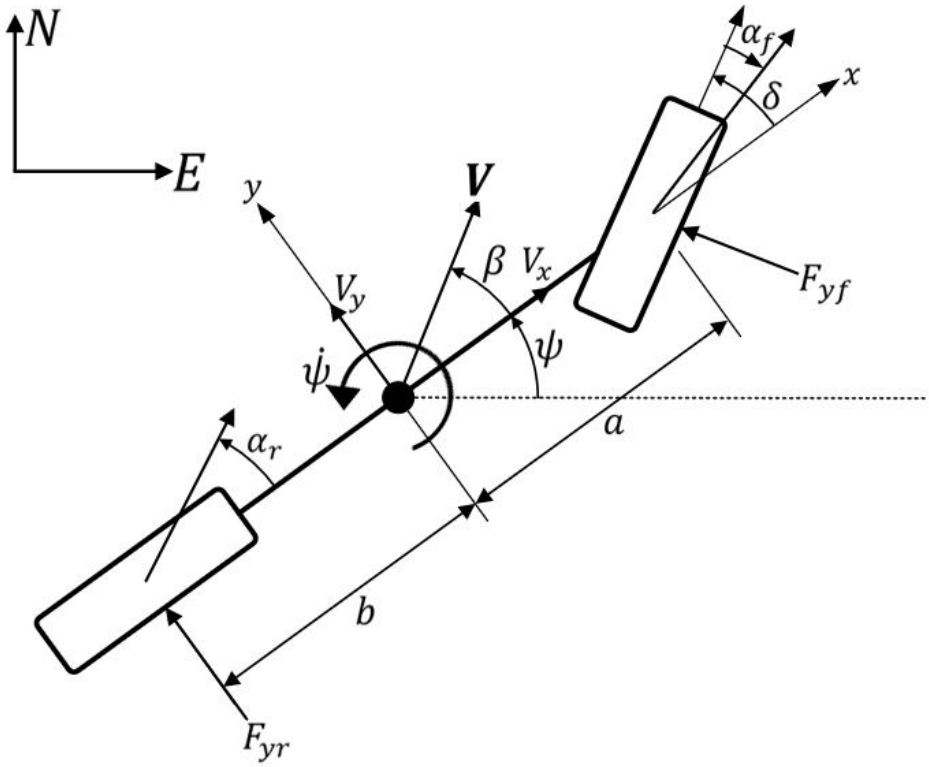

Figure 3.1: Lateral Dynamic Bicycle Model

than about 15 degrees. With these, and the previously defined assumptions, the linearized equations of motion of the vehicle are derived from Newtonian principles [15].

$$\dot{V}_y = -\frac{C_{\alpha f} + C_{\alpha r}}{mV_x} V_y + \left[\frac{-aC_{\alpha f} + bC_{\alpha r}}{mV_x} - V_x\right]\dot{\psi} + \frac{C_{\alpha f}}{m}\delta \tag{3.1}$$

$$\ddot{\psi} = -\frac{aC_{\alpha f} - bC_{\alpha r}}{I_z V_x} V_y - \frac{a^2 C_{\alpha f} + b^2 C_{\alpha r}}{I_z V_x}\dot{\psi} + \frac{aC_{\alpha f}}{Iz}\delta \tag{3.2}$$

The error equations for the controllers are based on the measurements described in Section 2.3, ΔY and θ_t. Note that F_4 is a user-defined transfer function which will be described in Chapter 4.

$$e_\psi = F_4\theta_t - \psi \tag{3.3}$$

$$e_Y = r - \Delta Y \tag{3.4}$$

The ego vehicle's velocity in the Y-direction of the reference path frame is

$$\dot{V_Y} = -V_x e_\psi + V_y \tag{3.5}$$

The $V_x e_\psi$ term is negative because it is defined based on the error to the path. Combining Equations (3.3) and (3.5) provides clarity on this.

$$\dot{V_Y} = V_x(\psi - \theta_t) + V_y \tag{3.6}$$

Since the ego velocity is resolved in the reference path frame instead of the global frame, the path tangent is subtracted from the vehicle yaw. Equation (3.6) is a typical linearized representation of the Y-velocity. For further detail on the derivation of these equations, see Appendix A.3 or [15].

3.2 Engine Torque Model

The longitudinal control of the vehicle is based on an engine torque model, as described by [16]. There are a few underlying assumptions in the development of the model: the transmission is at steady state (i.e., it is not performing a gear change), the torque converter is locked, and there is negligible longitudinal tire slip. The dynamics of the engine speed as it relates to a pseudo-input "net combustion torque", T_{net} is

$$\dot{\omega}_e = \frac{1}{J_e}\left(T_{net} - c_a R_g^3 r_{eff}^3 \omega_e^2 - R_g r_{eff} R_x\right) \tag{3.7}$$

where c_a is the aerodynamic drag coefficient, R_g is the gear ratio, r_{eff} is the effective wheel radius, R_x is the rolling resistance force. The effective engine inertia, J_e, given by

$$J_e = I_e + I_t + R_g^2 I_w + m R_g^2 r_{eff}^2 \tag{3.8}$$

where I_e is the engine inertia, I_t is the transmission inertia, I_w is the wheel inertia, and m is the vehicle mass. The engine speed is related to the motion of the vehicle by

$$\ddot{x} = r_{reff} R_g \dot{\omega}_e \tag{3.9}$$

For further explanation of the engine model, please see Appendix A.4 or [16].

3.3 System Identification

The vehicle used in simulation is the D-class sedan shown in Figure 3.2. The parameters of the vehicles are taken from CarSim (which is described in more detail in Section 5.1), and f_c is the control frequency. A control rate of 20 Hz was chosen

Figure 3.2: Simulation Vehicle.

because the bandwidth of the closed loop system (including the controllers designed in Chapter 4) is 0.458 Hz, which makes the control rate more than 40 times the bandwidth. This is important when considering signal aliasing, disturbance rejection, and effective tracking [1]. The mass, yaw inertia, and the distances from the axles to the CG may be pulled directly from a table in CarSim. CarSim provides tire information such as shear forces and moments, effective rolling radius, and rolling resistance moment information. It should be noted that the transmission inertia, I_t is an average of the inertias at each gear. The cornering stiffnesses require interpolation from the lateral force versus slip angle plot data, shown in Figure 3.3. The plot data provides the lateral force for a given slip angle for different vertical tire loads; it was

[1] See Section 8.4 of [17] for more details on sample rate selection.

Table 3.1: Vehicle Parameters

Parameter [units]	Value
f_c [Hz]	20
m [kg]	1370
I_z [kg-m^2]	2315.3
a [m]	1.11
b [m]	1.67
$C_{\alpha f}$ [kg-m/s^2]	64570.1
$C_{\alpha r}$ [kg-m/s^2]	51478
V_x [m/s]	22.352
R_δ	16.3785
R_g	1/4
R_v [h/km]	0.000026
R_c	0.0038
c_a	0.3
I_e [kg-m^2]	0.2
I_w [kg-m^2]	0
I_t [kg-m^2]	0.388
r_{eff} [cm]	32.5

created by CarSim using the Pacejka Magic formula tire model [2]. The cornering stiffnesses in Table 3.1 were calculated using a static vertical load. Since the weight split is known, the force on a single tire can be back calculated. Using only the linear portion of the tire curve (i.e., non-saturation driving conditions such as highway scenarios), cornering stiffnesses were found for the vertical loads above and below the vertical force calculated for a single tire. These were interpolated to get a cornering

[2]For more information on the Magic formula tire model, see [18]. For a brief explanation, see Section 13.5 in [16].

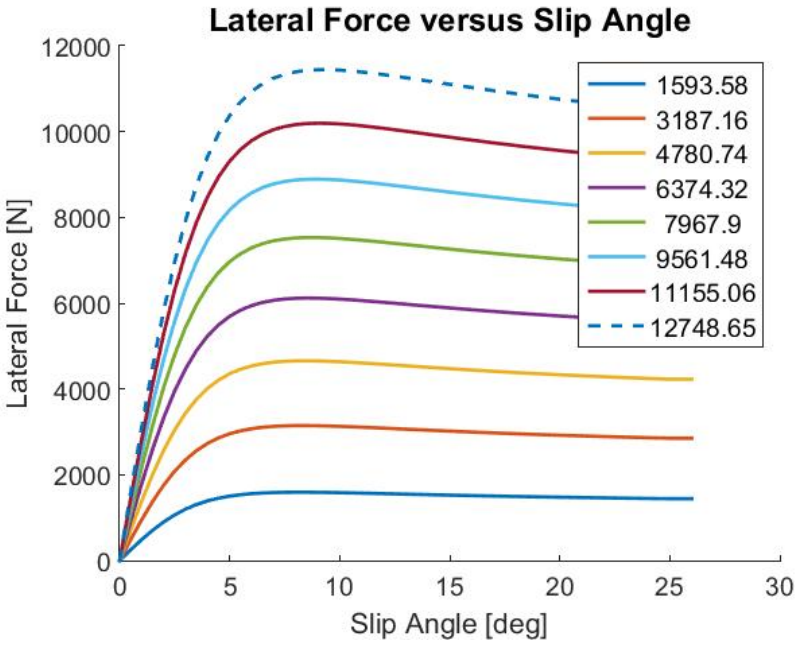

Figure 3.3: Lateral Force versus Slip Angle of a Single Tire for Multiple Vertical Loads from CarSim.

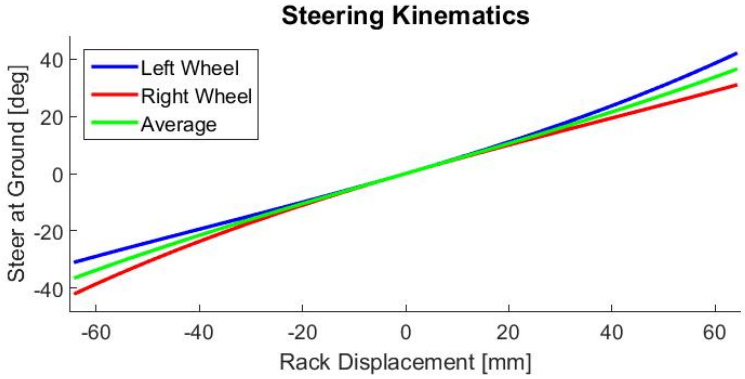

Figure 3.4: Steering Kinematics for the Left and Right Wheels from CarSim.

stiffness for a single tire. Because the bicycle model is used, the calculated cornering stiffness was doubled. This method was performed for the front and rear tires. The steering ratio, R_δ, was found using the average of the Pitman arm curves, shown in Figure 3.4. The difference in the left and right wheels is due to the Ackermann steering geometry. The vehicle used in the simulations has a powered rack and pinion

steering type; therefore, the steer ratio is calculated by

$$R_\delta = \left(\frac{M \times C}{360}\right)^{-1} = \left(\frac{0.5495 \dfrac{\text{deg at wheel}}{\text{mm on rack}} \times 40 \dfrac{\text{mm on rack}}{\text{rev at handwheel}}}{360 \text{ deg at handwheel}}\right)^{-1} \tag{3.10}$$

where the M is the slope of the average Pitman curve and C is the constant ratio between the rack and the pinion.

3.4 Conclusions

In this chapter, the vehicle model used in the controller design was presented. It is based on feedback of lateral position error and heading error. The errors were related to the lead vehicle's past positions. The engine model used in the design of the longitudinal controller was briefly described. Also, the parameters used in the control design were given. Finally, the cornering stiffnesses and the steer ratio used in simulation were calculated from CarSim tables.

Chapter 4

Cascaded Control Design for Lateral Following

The controller design follows a classical approach using both root locus and bode design. The controller designed has a cascaded architecture, which is portrayed in the two block diagrams below. The cascade is represented by the two loops in the each block diagram. The inner loop, containing $C_1(s)$, regulates the heading error and the outer loop, containing $C_2(s)$, regulates the lateral position error. The top diagram represents the control architecture as it appears for the ultimate lead vehicle. The information depicted by the two red lines are only available when the vehicle is

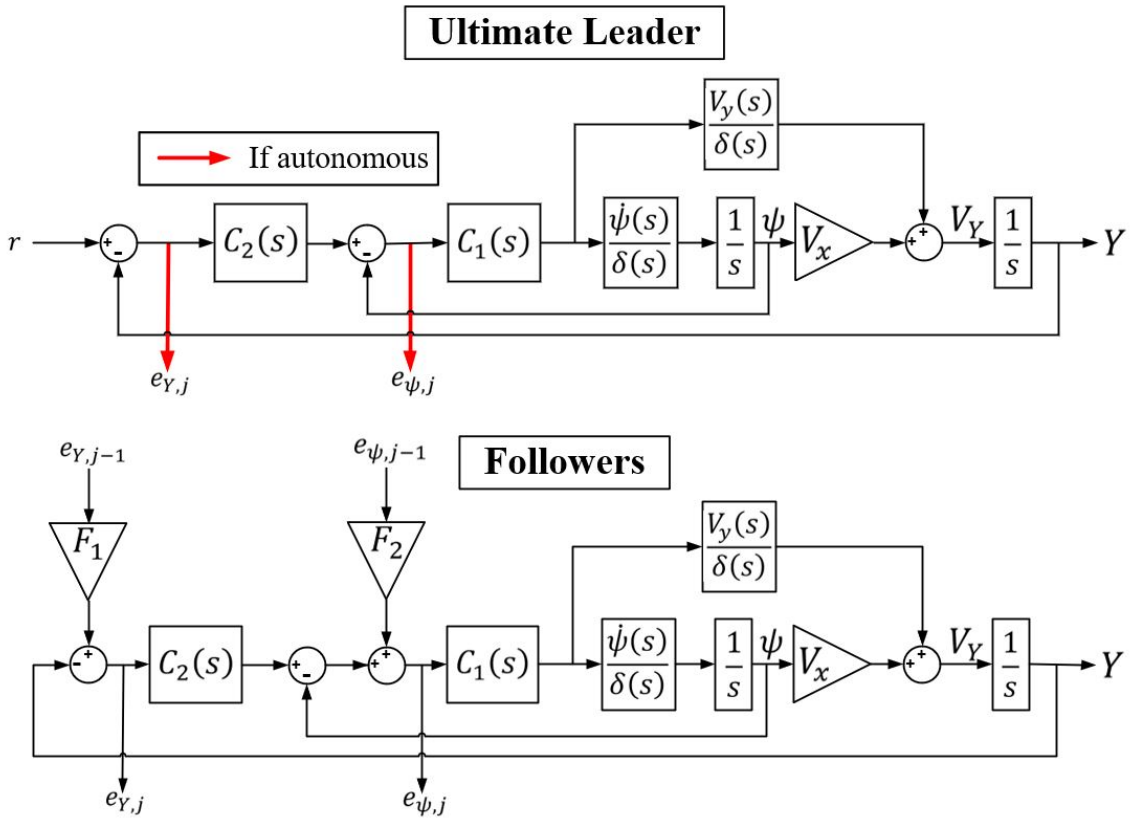

Figure 4.1: Two Vehicle Control Systems that each have a Cascaded Control Architecture.

being operated autonomously, not manually. The bottom diagram depicts the control architecture for all following vehicles. A cascaded design is helpful in that it allows one to separate the control problem into two simpler control problems. First, the inner loop controller, C_1, is designed, then treating the inner controller as part of the system, the outer controller, C_2, is designed. The outer controller provides a reference heading for the inner controller to follow. The linear transfer functions associated with the lead vehicle's lateral position error and heading error, F_1 and F_2, are selected by the user to ensure string stability. F_1 and F_2 are in the bottom block diagram of Figure 4.1. It should be noted that though Figure 4.1 depicts a continuous-time system, the control design was performed in discrete-time.

Before designing the inner loop controller, it is helpful to examine the poles and zeros of the open-loop system to better understand the original system response so that it is easier to see how the system has been changed by the controllers. Of course, these poles and zeros are not exactly the same as those of the real system because they are derived from the bicycle model. Figure 4.2 shows that there are two integrators. The zero at -1 is due to the discretization.

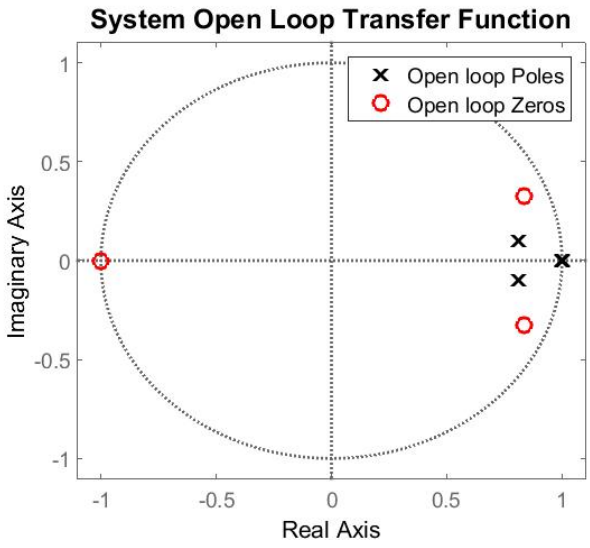

Figure 4.2: Original System Open Loop Transfer Function.

4.1 Inner Loop Design

The inner loop controller, C_1, is designed to regulate the yaw error to zero. It receives the yaw error based on the reference path, and adjusts it by the reference output from the outer controller, C_2. Firstly, the root locus of the inner loop transmission with $C_1 = 1$ was plotted, shown in Figure 4.3, to examine the possible closed-loop eigenvalues of the yaw dynamics with proportional control.

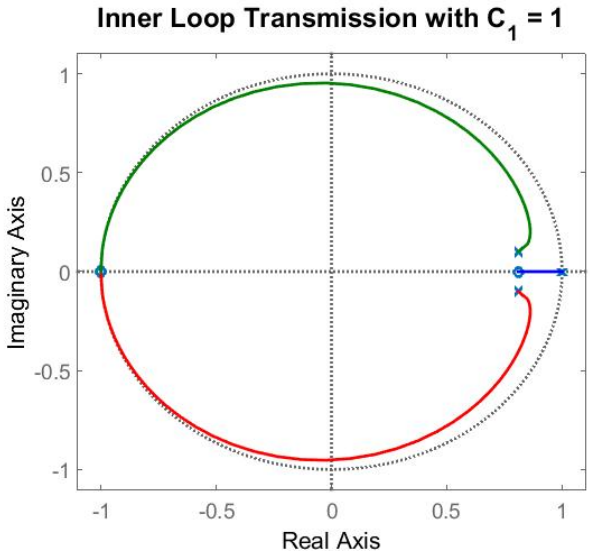

Figure 4.3: Root Locus of Inner Loop Transmission with $C_1 = 1$.

A lead compensator was then designed for the system. It is desired for the dominant eigenvalue to be real, so that the dominant response is that of a first order decay. For this system, a lead compensator produced a real dominant eigenvalue. A lead compensator was chosen over a PD controller for a couple reasons: a lead controller limits the amplification of high frequency noise and a lead compensator's pole is located such that it provides less derivative action and more smoothing. The lead compensator designed for this system is given by

$$C_1(z) = 2.03\frac{z - 0.75}{z - 0.2} \tag{4.1}$$

Including Equation (4.1) in the loop transmission transforms the root locus in Figure 4.3 to Figure 4.4. The potential closed-loop eigenvalues are all stable. After

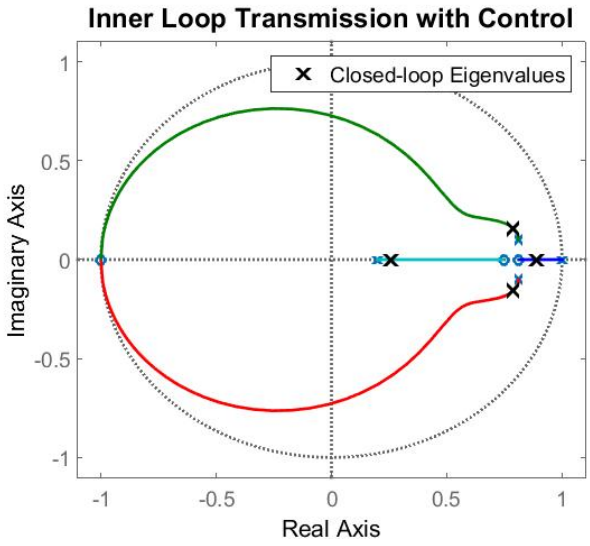

Figure 4.4: Root Locus of Inner Loop Transmission with Designed C_1.

selecting a gain, the inner loop was simulated to validate a satisfactory response. The step response of the inner loop is shown in Figure 4.5.

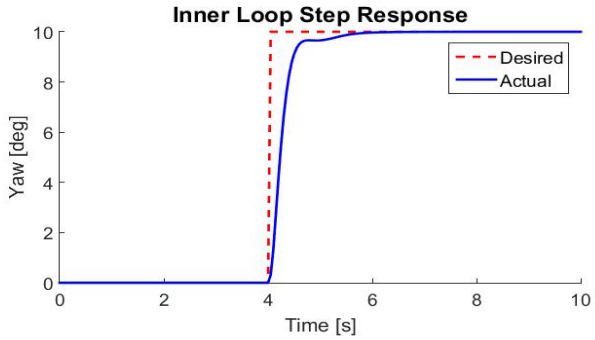

Figure 4.5: Step Response of the Inner Loop.

4.2 Outer Loop Design

The outer loop transmission combines the outer controller, the inner controller, the yaw dynamics, and the body-fixed lateral velocity dynamics. During the design of the outer controller, the inner controller was held constant. If the inner controller

is changed, the outer controller must be redesigned. The root locus of the outer loop transmission before the design of the outer controller (so it is set equal to 1) is shown in Figure 4.6.

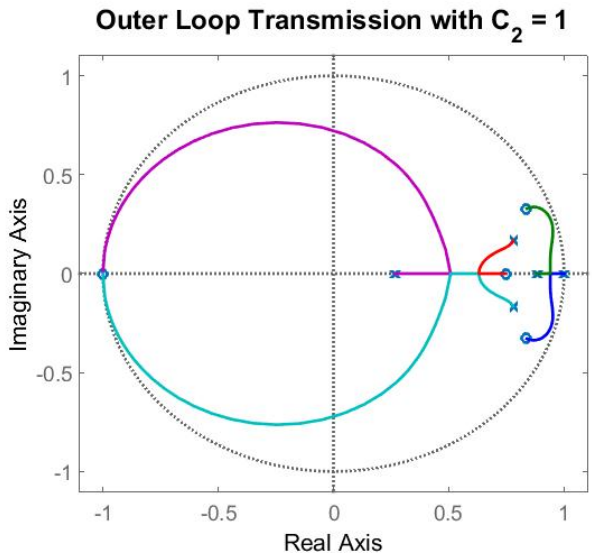

Figure 4.6: Root Locus of Outer Loop Transmission with $C_2 = 1$.

The outer controller is designed to output a reference yaw for the inner controller based on the lateral position error of the vehicle. There are two integrators embedded in the system which makes the system type 2 with regard to references, i.e., the system can track a ramp reference with zero steady-state error. However, in order to track in the midst of disturbances, the integrators must be in the controller not the system. Therefore, an integrator was added to the outer loop controller which makes it capable of tracking a step disturbance. After tuning, the final outer loop controller design is

$$C_2(z) = 0.0935\frac{z - 0.975}{z - 1} \tag{4.2}$$

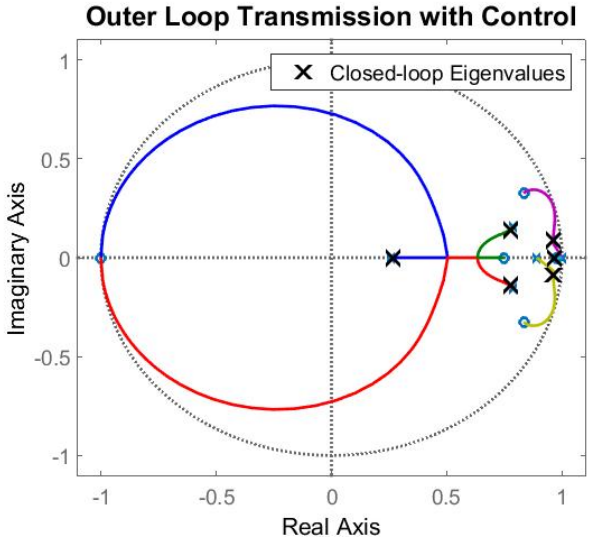

Figure 4.7: Root Locus of Outer Loop Transmission with Designed C_2.

4.3 Lateral String Stability

There are two main criteria related to string stability. The first criteria examines the gain of the transfer function from the lead vehicle's parameter of interest to the following vehicle's parameter of interest. For string stability, the transfer function must be less than or equal to one for all frequencies. In this thesis, the transfer function is from the path tangent of the lead vehicle, θ_1, to the heading error of the first follower, $e_{\psi,i}$. This criteria is expressed mathematically by

$$\left| \frac{e_{\psi,2}(j\omega)}{\theta_1(j\omega)} \right| \leq 1 \; \forall \; \omega \tag{4.3}$$

To evaluate the proposed controller design based on this criteria, the transfer function between the errors was found using Equation (3.3) and the bottom block diagram in Figure 4.1. This transfer function is given by Equation (4.4).

$$\left| \frac{e_{\psi,2}}{\theta_1} \right| = \frac{F_3 s^2 + F_3 \dfrac{V_y}{\delta} C_1 C_2 s}{s^2 + \left(\dfrac{\dot{\psi}}{\delta} C_1 + \dfrac{V_y}{\delta} C_1 C_2 \right) s + V_x \dfrac{\dot{\psi}}{\delta} C_1 C_2} \tag{4.4}$$

The Laplace notation "(s)" was dropped in Equation (4.4) for simplicity. F_3 is a user-defined linear function. Evaluating Equation (4.4) using the values in Table 3.1 and setting F_2 equal to a low-pass filter with a bandwidth of 2 rad/s yields

$$\left|\frac{e_{\psi,2}}{\theta_1}\right| = \frac{2s^6 + 80.59s^5 + 584.2s^4 + 1450s^3 - 1811s^2 - 905.5s}{s^7 + 42.29s^6 + 435.5s^5 + 2463s^4 + 7201s^3 + 1.34\text{e}4s^2 + 1.49\text{e}4s + 5562} \tag{4.5}$$

If the criterion in Equation (4.3) is met, the type of string stability is known as l_2 string stability. This type is considered a weak form of string stability because it only guarantees that the maximum error is dampened along the string. Note that Equation (4.5) is represented using continuous time because the gain plot is represented more clearly in continuous time. In discrete time, the gain plot is presented from $0 - \pi$ times the sample time which is not as clear as the continuous time frequency spectrum.The gain plot of the transfer function when F_3 is equal to 1 versus when F_3 is equal to the low-pass filter is shown in Figure 4.8.

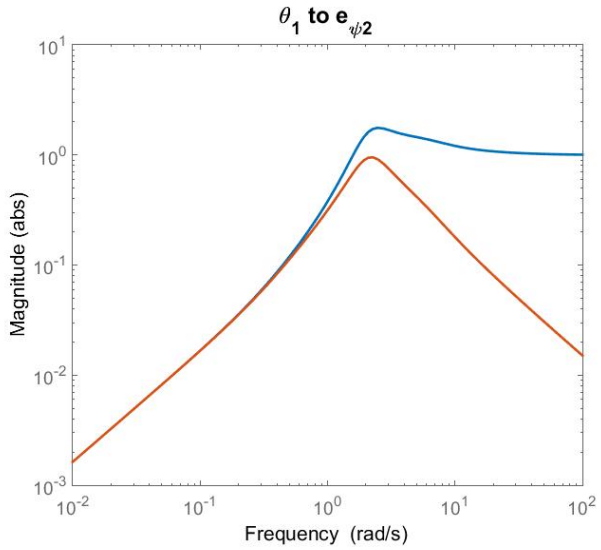

Figure 4.8: Gain from Lead Vehicle Path Tangent to First Follower Vehicle Heading Error.

The second criteria is that the closed-loop system must have a sign-invariant impulse response[1]. This translates mathematically as

$$e_{Y,i}(t) > 0 \, , \; t \to \infty \tag{4.6}$$

If both Equation (4.3) and Equation (4.6) hold, then a strong sense of lateral string stability is held, denoted as l_∞. To ensure a sign-invariant impulse response, a pre-filter, F_2, was applied to the heading error passed to the first following vehicle if the ultimate lead is autonomously driven or to the second following vehicle if the ultimate lead is manually driven. The prefilter used is a low-pass filter with a bandwidth of 6 rad/s, given in Equation (4.7). Note that the string stability criteria are met when $F_1 = 1$, so there is no need to design a prefilter for the lead vehicle's lateral position error.

$$F_2 = \frac{0.2592}{z - 0.7408} \tag{4.7}$$

4.4 Longitudinal Control

Although longitudinal control is not the focus of this thesis, a basic ACC system was implemented so that the vehicles in the convoy could be initialized near each other, then follow each other at a set distance. This is to address the initialization problem described in Section 2.3. The lower level of the longitudinal controller is based on the engine torque model described in Section 3.2. The objective of the lower level controller is to calculate an engine torque, T_{net}, that will track a desired acceleration. Solving Equation (3.7) for T_{net} and substituting in Equation (3.9) gives

$$T_{net} = \frac{J_e}{R r_{eff}} \ddot{x}_{des} + \left[c_a R^3 r_{eff}^3 \omega_e^2 + R\big(r_{eff} R_x + T_{br}\big) \right] \tag{4.8}$$

[1]For more information on achieving a sign-invariant response to an impulse reference, see [19], [20], and [21].

where $\ddot{x}_{des}$ is the desired acceleration determined by the high level controller. The braking torque, T_{br}, was neglected because braking scenarios are not addressed in this thesis. The rolling resistance force is calculated using

$$R_x = F_z R_{surf}(R_c + R_v V_x) \tag{4.9}$$

where F_z is the vertical load on the tire, R_{surf} is the road surface effects coefficient, R_c is the constant rolling resistance coefficent, and R_v is the speed varying rolling resistance coefficient. These parameters are available in CarSim, or they may be estimated in real-time by performing coast-down tests. Using the coefficients values listed in Table 3.1, $R_{surf} = 1$, calculating static vertical loads, and a longitudinal velocity of 22.4 m/s, the total rolling resistance force is 79.2 N. Since the force does not affect the ability of the controller to match the leader's longitudinal velocity and achieve a desired following distance (this is shown in Section 5.2), it is neglected.

The high level adaptive cruise controller uses the constant time-gap (CTG) spacing policy described in [16] with a slight modification. The spacing error includes a desired inter-vehicle spacing, L_{des}, instead of the length of the preceding vehicle, l_{j-1}.

$$\xi_j = \epsilon_j + h\dot{x}_j \tag{4.10}$$

where

$$\epsilon_j = \rho_{j,j-1} - L_{des} \tag{4.11}$$

with ρ being the current separation distance between vehicles j and $j-1$. The CTG control law, as developed by [22], is

$$\ddot{x}_{j,des} = -\frac{1}{h}\left(\dot{\epsilon}_j + \zeta\xi_j\right) \tag{4.12}$$

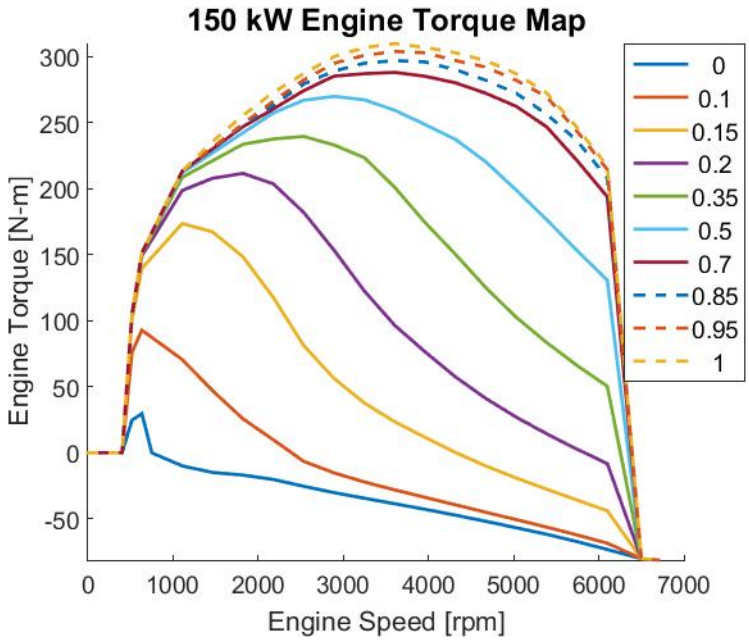

Figure 4.9: Engine torque versus Engine Speed for 10 Throttle Positions from CarSim.

where $\zeta > 0$ and is chosen by the user to meet performance specifications. Optimizing the longitudinal control was not a focus in this thesis; the only requirement is that it could maintain a separation distance for the evaluation of the lateral controllers.

The lower level control variable, T_{net} is mapped to throttle position using the current engine speed, ω_e, via torque tables provided by CarSim, shown in Figure 4.9. The throttle positions vary from 0-1, with 0 being no throttle and 1 being full throttle. The vehicle parameters used in the design of the longitudinal controller are outlined in Table 4.1.

Table 4.1: Longitudinal Control Parameters

Parameter [units]	Value
h [s]	2
ζ	0.25
L_{des} [m]	300

4.5 Convoy Following Strategies

In this thesis, two following strategies are considered: following the immediate lead and following the ultimate lead. To ensure there is no confusion in notation with regard to the convoy in following sections, the diagrams in Figures 4.10 and 4.11 illustrate what is meant by these terms. Why the information being passed back to following vehicles will be explained in Section 4.3.

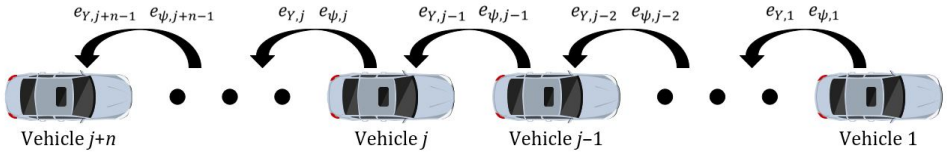

Figure 4.10: Immediate Lead Following Architecture.

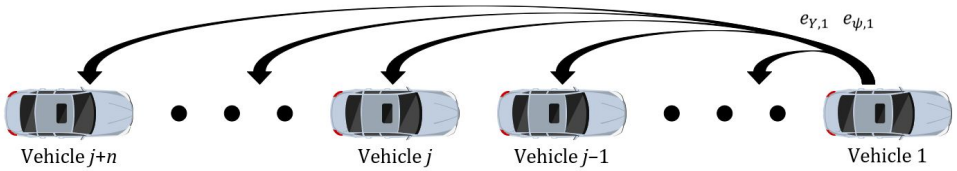

Figure 4.11: Ultimate Lead Following Architecture.

4.6 Conclusions

In this chapter, a discrete cascaded controller was developed which uses feedback of heading offset and lateral offset from a reference path for path following. It was also shown that when a leader shares its heading offset and lateral offset information to its follower, then a string stable controller may be achieved. Also, a longitudinal controller which uses constant time-gap policy was presented. The outputted torque from the controller was also mapped to a throttle position by using the current engine speed. Finally, the two convoy architectures examined in this thesis were illustrated.

Chapter 5

Simulation

The simulation environment is a combination of Simulink and CarSim. Three scenarios are considered: a single lane change, a double lane change, and the National Center for Asphalt Technology (NCAT) test track with bank angle. In each scenario, two different vehicle following architectures are evaluated: ultimate lead following and immediate lead following (as described in Section 4.5). In conjunction with these architectures, a manually driven and an autonomously driven ultimate lead vehicle are considered. The simulations that are performed for each scenario are diagramed in Figure 5.1. Therefore, a total of 5 control schemes are examined for

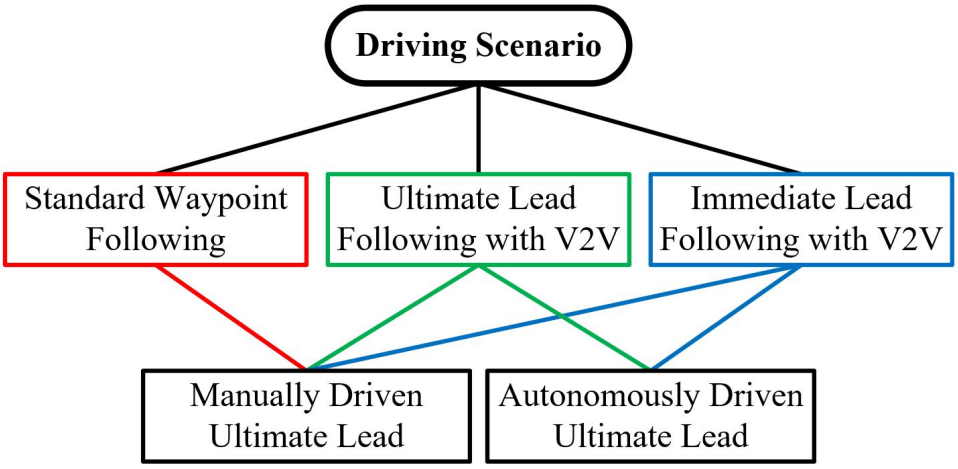

Figure 5.1: Simulation Scenarios Diagram.

each of the 3 scenarios giving a total of 15 simulation sets. The lateral error is the state compared among the scenarios. The ability of the longitudinal controller to maintain a separation distance is illustrated. White noise with the standard deviations described in Section 2.4 are applied to the simulated DRTK and TDCP measurements.

5.1 Simulation Environment

5.1.1 Simulink

Simulink gives users the ability to design controllers and estimators using a block diagram interface. It helps visualize the process, from receiving measurements to calculating the control input. Simulink comes with a library of function blocks including standard controllers. There are even more options when toolboxes are purchased. For instance, there is a Model Predictive Control (MPC) block included with the Control System Toolbox. However, the controllers implemented in this thesis do not use any built-in controller blocks.

In Figure 5.2, a top level view of the simulink model used in this work is shown. Simulink allows the user to create subsystems so that the elements associated with a particular system may be separated from another system. Figure 5.3 looks inside the

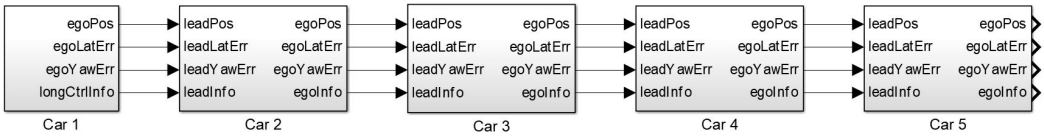

Figure 5.2: Simulink Model of All Vehicles.

Car 2 subsystem. Inside the subsystem, there are the two controller blocks: "Lateral Position Control" and "Yaw Control". The CarSim S-Function block is preceded by a memory block, which is used so that there is not an algebraic loop in the model. After the CarSim block is a rate transition block. The CarSim block is running at 1000 Hz, so the rate transition block is used to reduce the sample rate to 20 Hz, which is the controller sampling frequency. The DRTK and TDCP measurements are calculated in the "RPV & Odometry" block, and they are passed into the "Path Duplication" block. This is where the lateral offset and path tangent measurements are calculated. Also, the leader's past lateral offset and heading offset are stored in this block. The longitudinal control is performed in the "ACC" block. This block

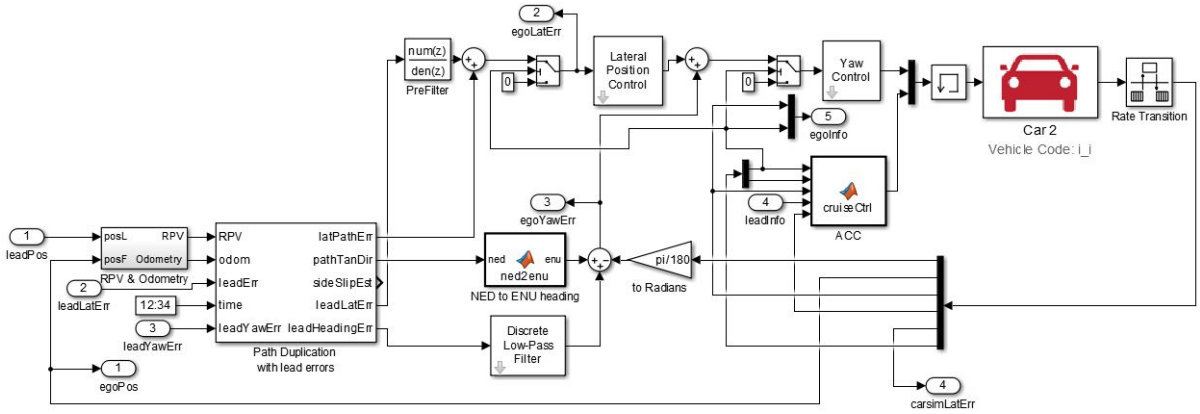

Figure 5.3: Simulink Model of a Single Vehicle.

and the "NED to ENU heading" block are MATLAB function blocks, which means that MATLAB code may be written inside them.

5.1.2 CarSim

CarSim is a high-fidelity vehicle simulation software. The strength behind the CarSim software is the fact that its vehicle models have been experimentally validated using real vehicles [23]. Powertrain, brake, steering, suspension, and tire dynamics are all taken into account in the CarSim model. CarSim also allows the user to create custom vehicles in its workspace. The software outputs around 800 different outputs of the vehicle motion and environment, including position, velocities, rotation rates, attitude, tire forces, engine torque, and accelerations. The home screen of the software graphical user interface (GUI) is shown in Figure 5.4.

Another strength of the software is its ability to be integrated into a Simulink model via an S-function block. This allows users to design controllers based on CarSim vehicle models and test them using Simulink. The user can provide the CarSim block with inputs such as: steering wheel angle, brake pressures, and transmission gear. Users may also define the terrain their vehicle is travelling on. For instance, Auburn has designed the National Center for Asphalt Technology (NCAT) test track into the CarSim environment. It is 1.71 miles long with 8 degrees of bank in the turns.

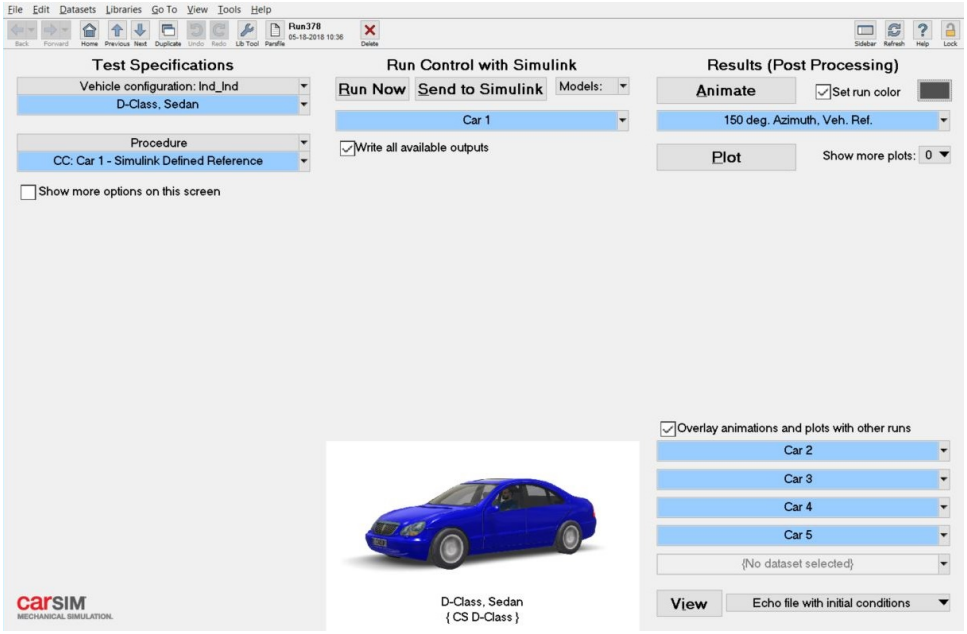

Figure 5.4: CarSim GUI

Figure 5.5: Actual and Simulated NCAT Test Track.

5.2 Longitudinal Control

The longitudinal control of the ultimate lead vehicle was controlled using CarSim's built in speed controller. All of the following vehicles used the longitudinal

controller described in Section 4.4. The velocity response versus time of the vehicles and the range between the vehicles are shown in Figure 5.6 and Figure 5.7, respectively. The following vehicles were allowed to travel at idle speed while their lead vehicle gained speed. In Table 4.1, the desired following distance is listed as 300 m. The extra 25 m in Figure 5.7 is due to the time headway.

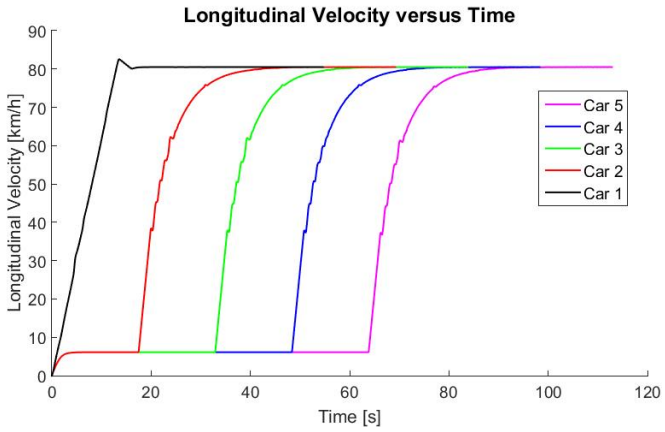

Figure 5.6: Longitudinal Velocity Response of the Convoy.

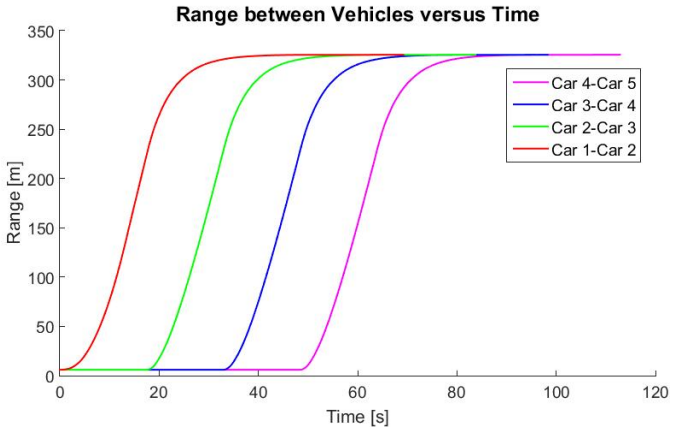

Figure 5.7: Range between Vehicles.

5.3 Standard Waypoint Following

In standard waypoint following, the following vehicles only use the DRTK/TDCP solutions in order to follow a virtual lead vehicle. They receive no further information

from the lead. A single lane change of 3.5 m is performed using ultimate lead following and immediate lead following.

5.3.1 Ultimate Lead Following

This is the waypoint method used by most convoys for lateral control. The ultimate lead is followed without any additional information. Figures 5.14-5.16 show that the convoy remains stable. The small variations between the paths of the following vehicles are due to noise and calculating the offsets from the path from different positions. Figure 5.15 shows a maximum lateral offset of about 1 m for all of the following vehicles. The steering wheel angle is very noisy. This is due to the fact that there is no damping between the control input and the vehicles actual steering wheel. The steering changes are instantaneous.

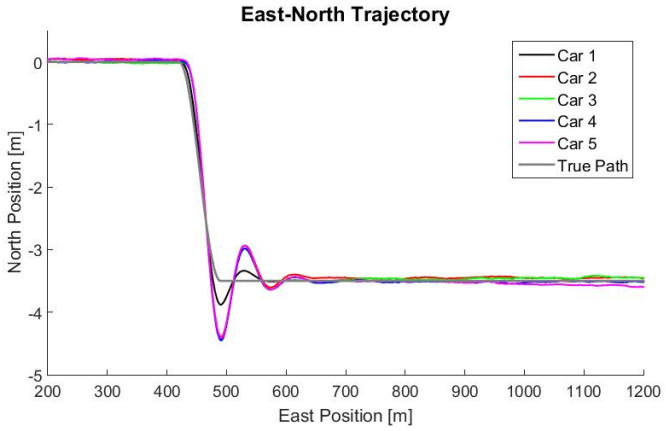

Figure 5.8: East-North Trajectory for Standard Ultimate Lead Waypoint Following

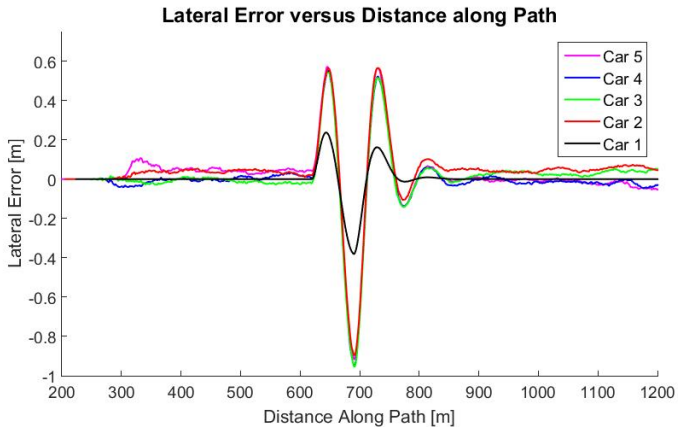

Figure 5.9: Lateral Offset for Standard Ultimate Lead Waypoint Following

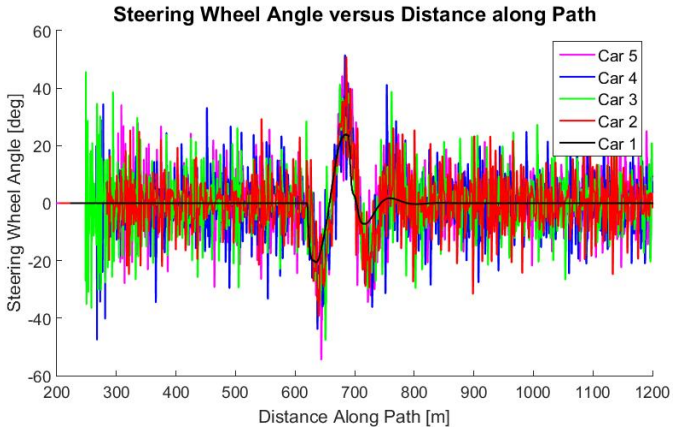

Figure 5.10: Steering Wheel Angle for Standard Ultimate Lead Waypoint Following

5.3.2 Immediate Lead Following

Standard waypoint following of the immediate lead is not used in convoys because it becomes unstable very quickly. The same single lane change scenario except that the immediate lead is followed instead of the ultimate lead. As can be seen from Figures 5.11-5.13, the convoy becomes increasingly unstable down the string with the 5th vehicle being unstable.

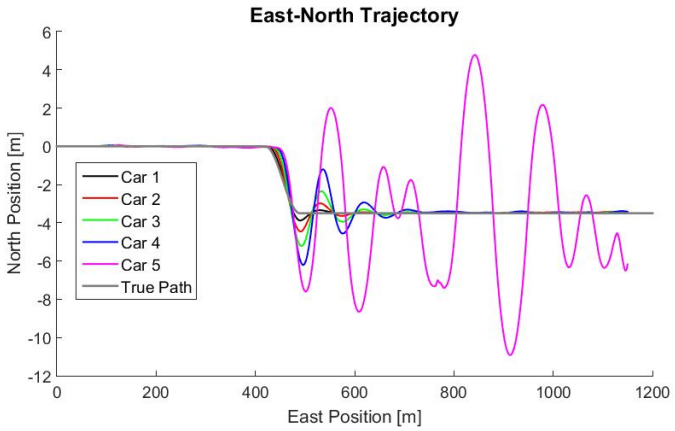

Figure 5.11: East-North Trajectory for Standard Immediate Lead Waypoint Following

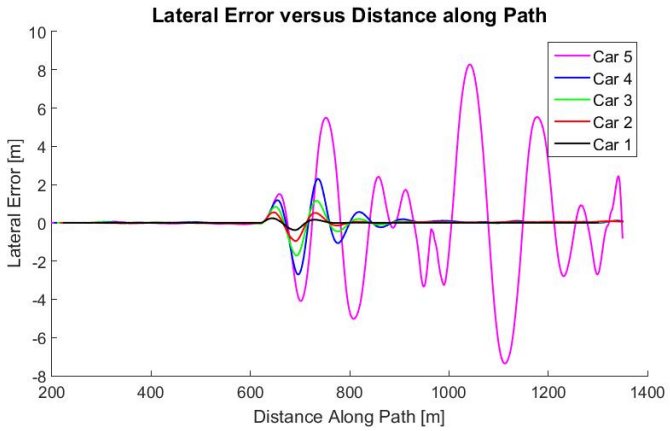

Figure 5.12: Lateral Offset for Standard Immediate Lead Waypoint Following

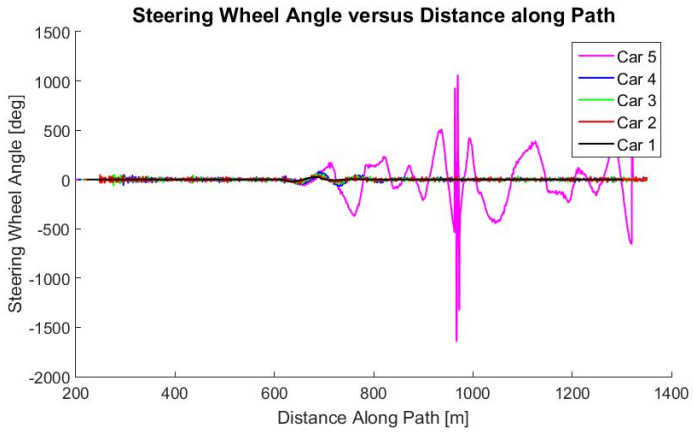

Figure 5.13: Steering Wheel Angle for Standard Immediate Lead Waypoint Following

5.4 Manually Driven Ultimate Lead

In most convoying scenarios, especially in current day, the ultimate lead is manually driven and all of the following vehicles are autonomous. In the simulation

environment, this means that the ultimate lead vehicle's lateral offset and heading offset is unknown to the following vehicles.

5.4.1 Single Lane Change

Ultimate Lead Following

The ultimate lead following for a single lane change is the standard method shown in Section 5.3.1, so it is not shown again here.

Immediate Lead Following

Shown in Figures 5.14-5.16 is a convoy for which each following vehicle has knowledge of its immediate lead's lateral offset and heading offset. Again, the ultimate lead is manually driven. Therefore, the second vehicle in the convoy does not have information regarding the lead's lateral offset and heading offset. However, from Figure 5.15, the lateral offsets along the string are decreasing.

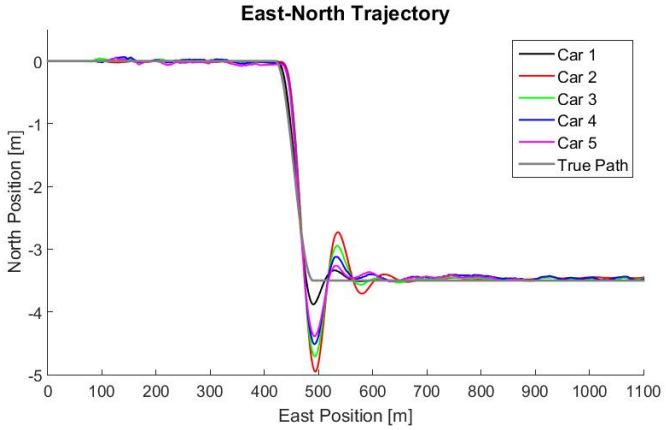

Figure 5.14: East-North Trajectory for Immediate Lead Following with Manual Ultimate Lead

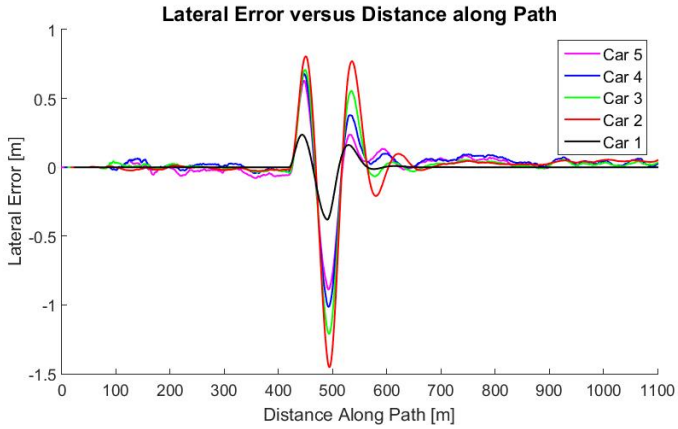

Figure 5.15: Lateral Offset for Immediate Lead Following with Manual Ultimate Lead

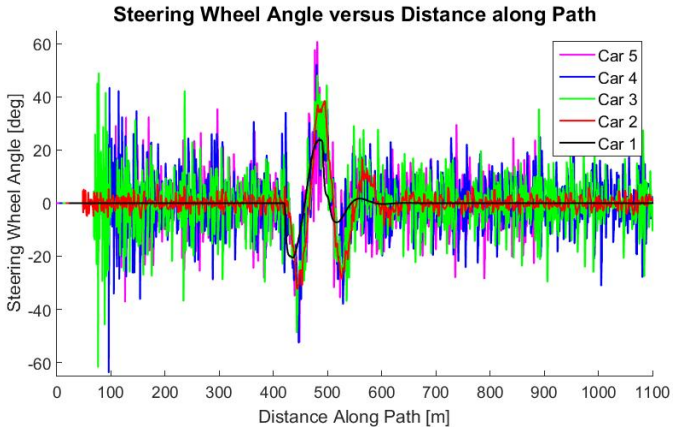

Figure 5.16: Steering Wheel Angle for Immediate Lead Following with Manual Ultimate Lead

5.4.2 Double Lane Change

A double lane change is a standard maneuver for testing stability and safety. During this maneuver, the vehicle exhibits high lateral dynamics.

Ultimate Lead Following

In the ultimate lead following architecture, the maximum lateral offset was just under 1 m. The responses are shown in Figures 5.17-5.19.

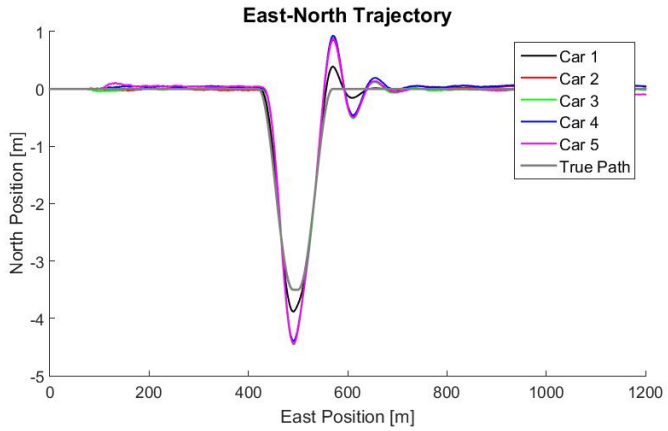

Figure 5.17: East-North Trajectory for Ultimate Lead Following with Manual Ultimate Lead

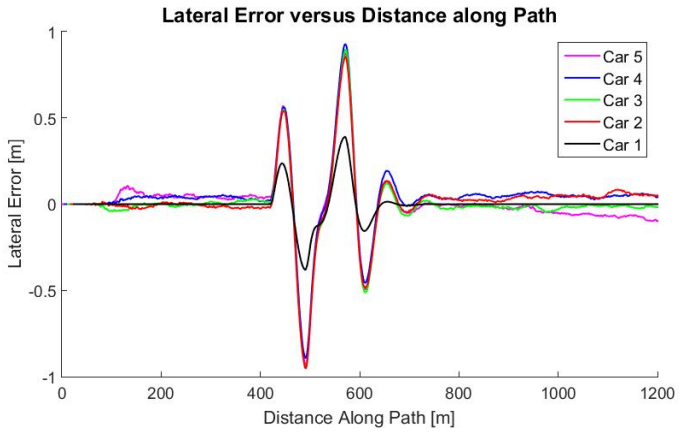

Figure 5.18: Lateral Offset for Ultimate Lead Following with Manual Ultimate Lead

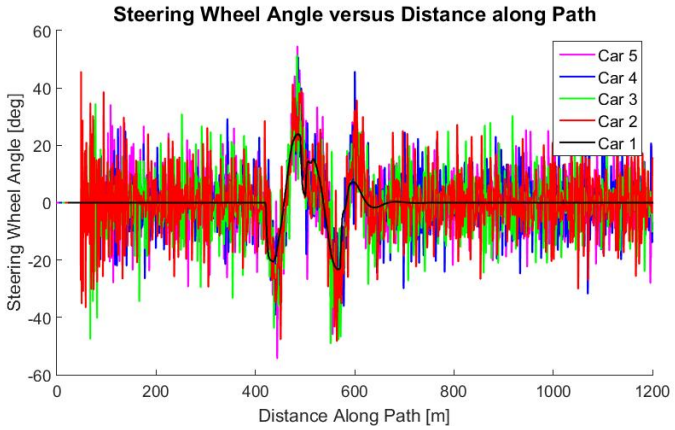

Figure 5.19: Steering Wheel Angle for Ultimate Lead Following with Manual Ultimate Lead

Immediate Lead Following

In the immediate lead following architecture, the maximum lateral offset was just under 1 m as well. However, the steady state error in the immediate lead scenario, shown in Figure 5.21, is smaller than in the ultimate lead following scenario, shown in Figure 5.18.

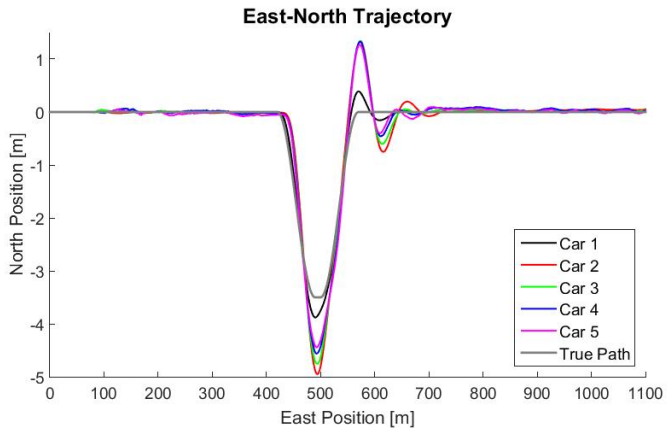

Figure 5.20: East-North Trajectory for Immediate Lead Following with Manual Ultimate Lead

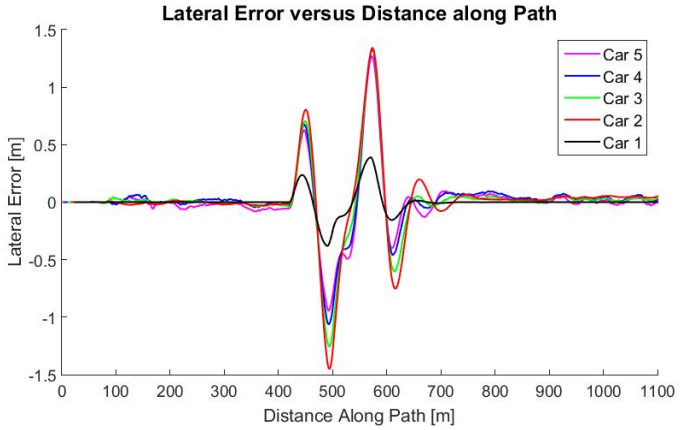

Figure 5.21: Lateral Offset for Immediate Lead Following with Manual Ultimate Lead

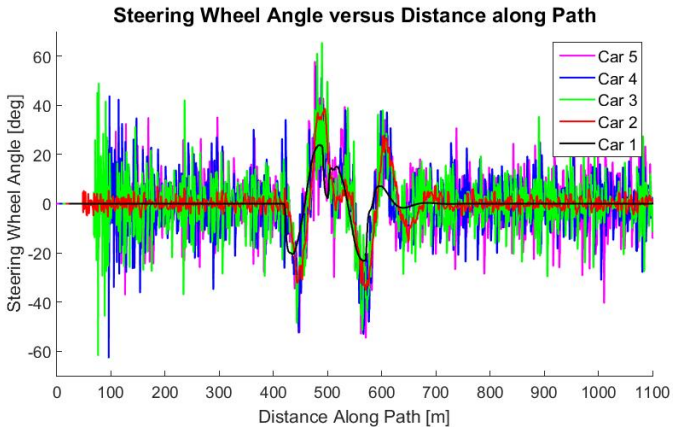

Figure 5.22: Steering Wheel Angle for Immediate Lead Following with Manual Ultimate Lead

5.4.3 NCAT Test Track - Banked

As mentioned earlier, the NCAT track is a 1.71 mile long test track with an 8 degree bank in the turns. This shows how the convoy responds to an external disturbance. For these tests, only the first two turns of the track are examined.

Ultimate Lead Following

When following the ultimate lead, there was a maximum lateral offset of about 1.5 m. The trajectories, lateral offsets, and steering wheel angles are shown in Figures 5.23-5.25.

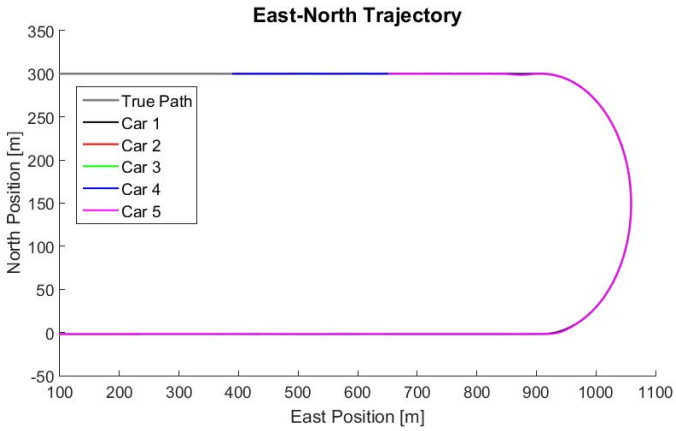

Figure 5.23: East-North Trajectory for Ultimate Lead Following with Manual Ultimate Lead

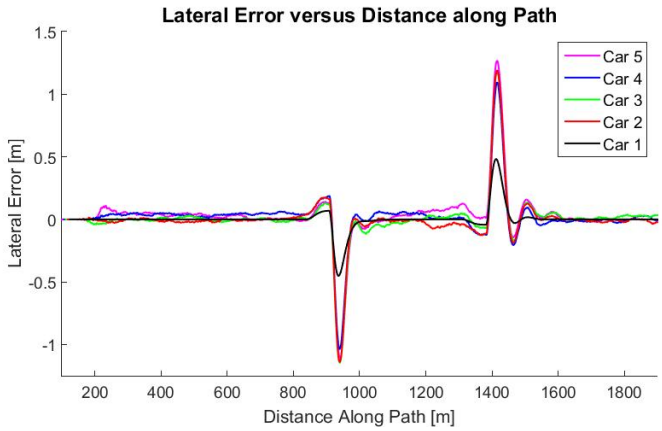

Figure 5.24: Lateral Offset for Ultimate Lead Following with Manual Ultimate Lead

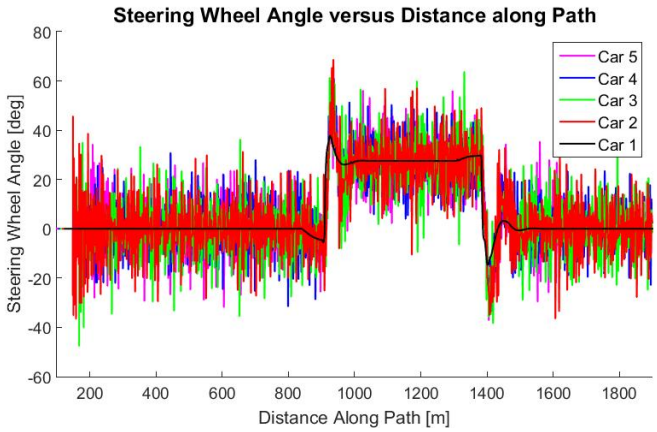

Figure 5.25: Steering Wheel Angle for Ultimate Lead Following with Manual Ultimate Lead

Immediate Lead Following

In the immediate lead following scenario, the maximum lateral offset is about 1.25 m. These results are shown in Figures 5.26-5.28.

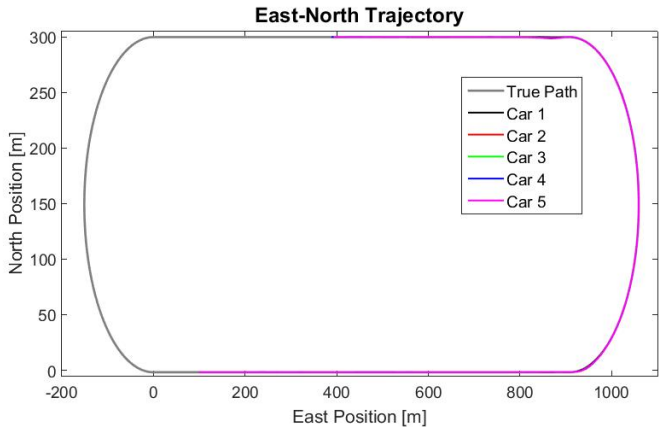

Figure 5.26: East-North Trajectory for Immediate Lead Following with Manual Ultimate Lead

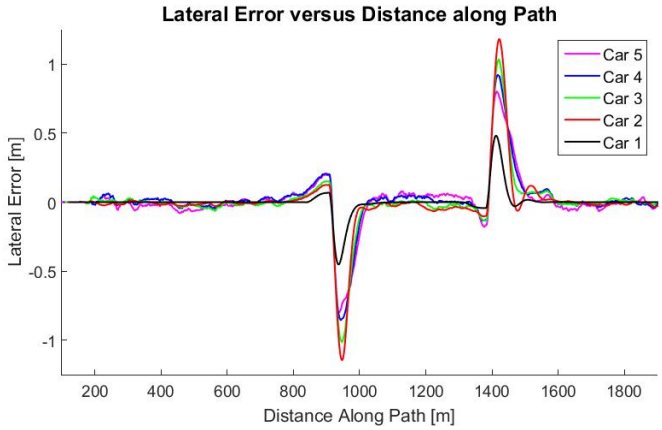

Figure 5.27: Lateral Offset for Immediate Lead Following with Manual Ultimate Lead

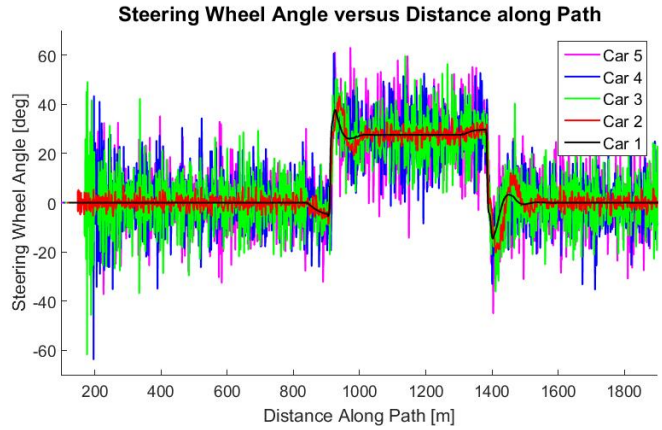

Figure 5.28: Steering Wheel Angle for Immediate Lead Following with Manual Ultimate Lead

5.4.4 Immediate Lead versus Ultimate Lead Evaluation

The lateral offset comparison for each of the scenarios are shown in Figures 5.29-5.31. From these graphs, it shown that the immediate lead following and ultimate lead following have very similiar responses. At some points the vehicles following their immediate lead have a smaller lateral offset, and at other points the vehicles following the ultimate lead have a smaller lateral offset. Based on this, both following schemes seem like feasible options depending on the situation at hand. In typical highway scenarios, it may seems more feasible to follow the immediate lead, so that the immediate lead does not have to continually broadcast the ultimate leads information.

Car 1 and Car 2's trajectories for ultimate lead following and immediate lead following are the same because in either scenario the following situation does not change for the first two vehicles.

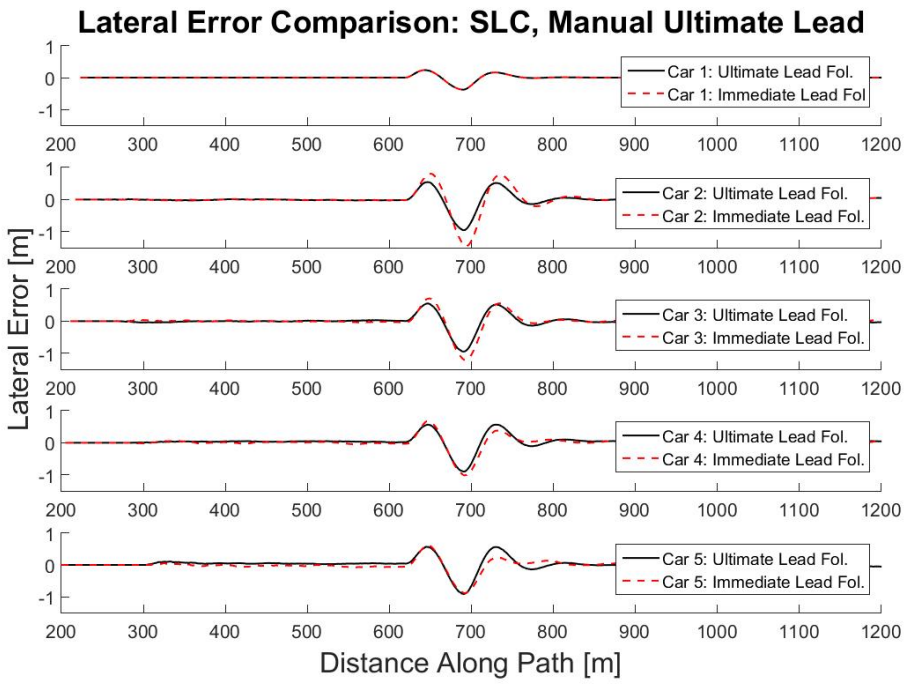

Figure 5.29: Lateral Offset Comparison for Single Lane Change, Manually Driven Lead.

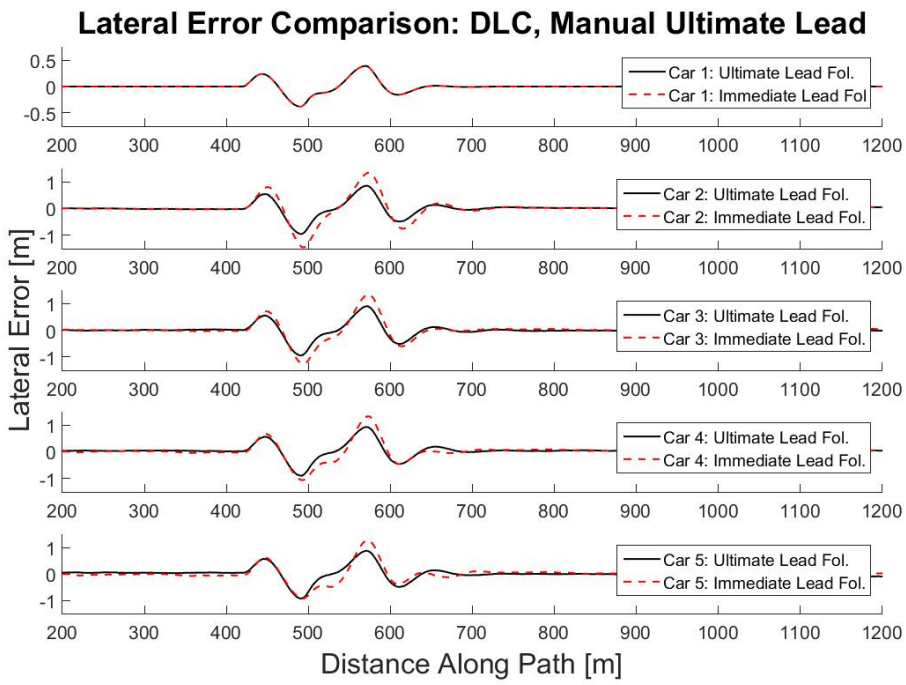

Figure 5.30: Lateral Offset Comparison for Double Lane Change, Manually Driven Lead.

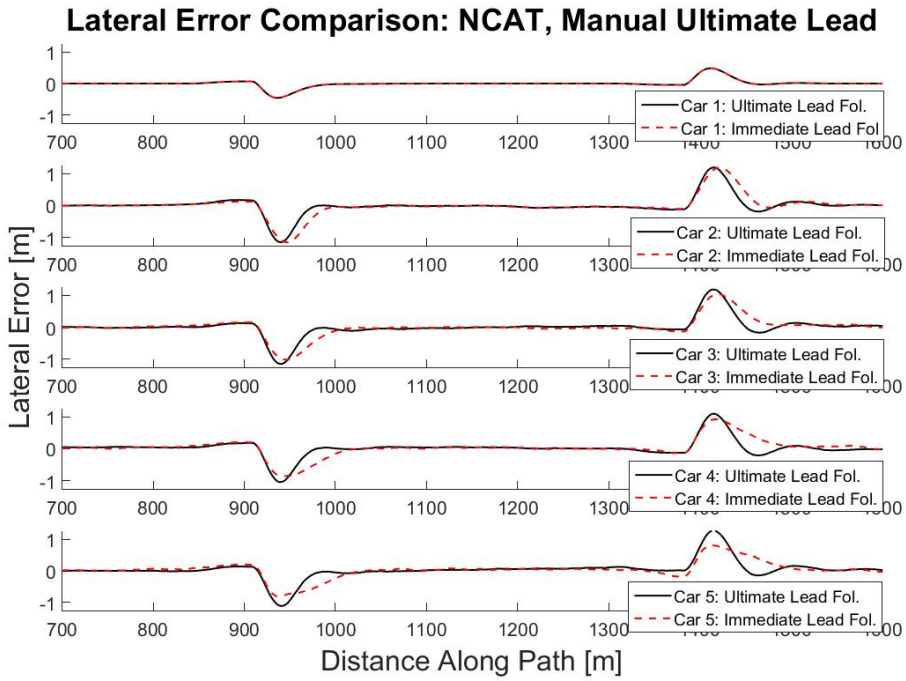

Figure 5.31: Lateral Offset Comparison for Double Lane Change, Manually Driven Lead.

5.5 Autonomously Driven Ultimate Lead

As vehicles move towards full autonomy, it is important to consider the case where the ultimate lead vehicle is autonomous. Since the ultimate lead is autonomously driven, the following vehicles have knowledge of the ultimate lead vehicle's lateral offset and heading offset. The following subsections present the results for when the ultimate lead is autonomously driven. The same scenarios that were performed with a manually driven ultimate lead are repeated here.

5.5.1 Single Lane Change

Ultimate Lead Following

Again, in this following scheme, all of the following vehicles follow the ultimate lead. The results for the single lane change using ultimate lead following are shown in Figures 5.32-5.34. The maximum lateral offset is about 0.4 m, as compared to the nearly 1 m lateral offset in the manually driven ultimate lead case.

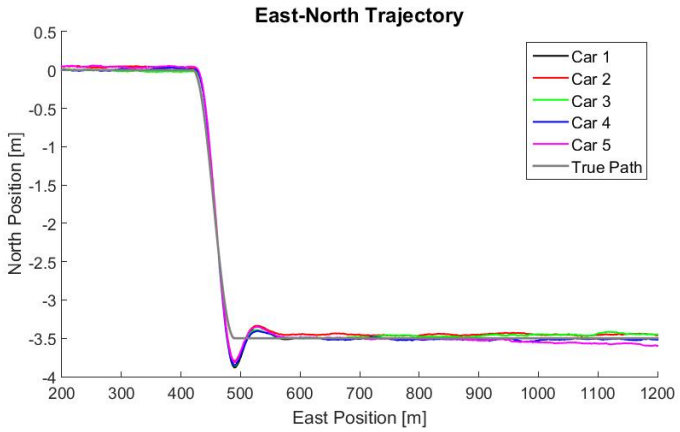

Figure 5.32: East-North Trajectory for Ultimate Lead Following with Autonomous Ultimate Lead

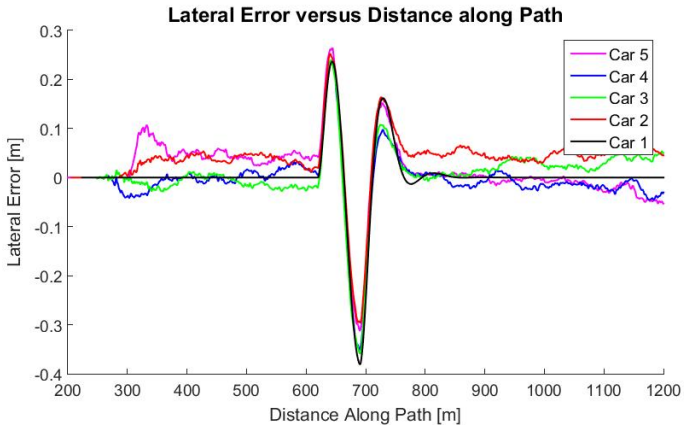

Figure 5.33: Lateral Offset for Ultimate Lead Following with Autonomous Ultimate Lead

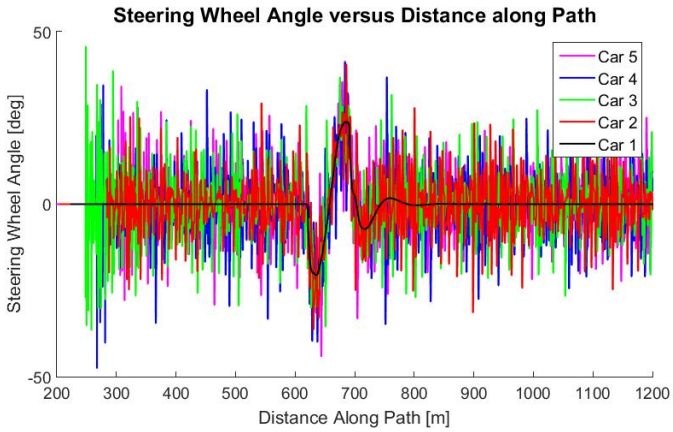

Figure 5.34: Steering Wheel Angle for Ultimate Lead Following with Autonomous Ultimate Lead

Immediate Lead Following

Now consider the architecture where each vehicle follows its immediate lead. Although, the second vehicle has a larger lateral offset than the preceding vehicle, it can be seen in Figure 5.36 that the lateral offset is being dampened for the rest of the vehicles.

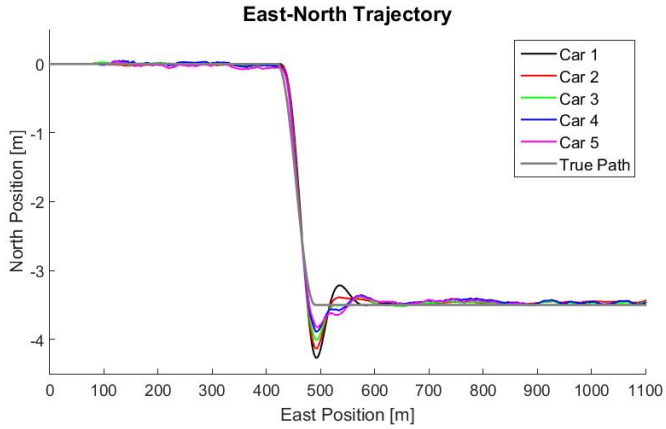

Figure 5.35: East-North Trajectory for Immediate Lead Following with Autonomous Ultimate Lead

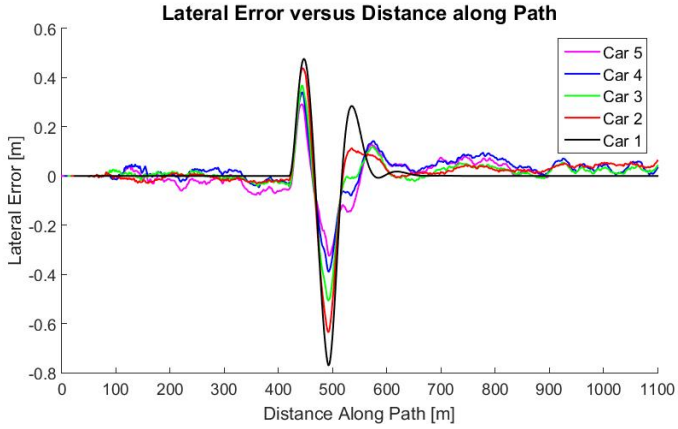

Figure 5.36: Lateral Offset for Immediate Lead Following with Autonomous Ultimate Lead

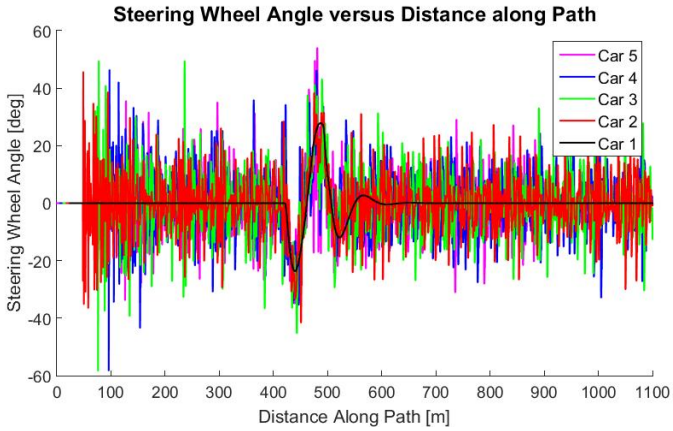

Figure 5.37: Steering Wheel Angle for Immediate Lead Following with Autonomous Ultimate Lead

5.5.2 Double Lane Change

Ultimate Lead Following

The same double lane change is performed; however, when the ultimate lead's lateral offset and heading offset are known, the maximum lateral offsets for the rest of the vehicles in the convoy are halved. These results are shown in Figures 5.38-5.40.

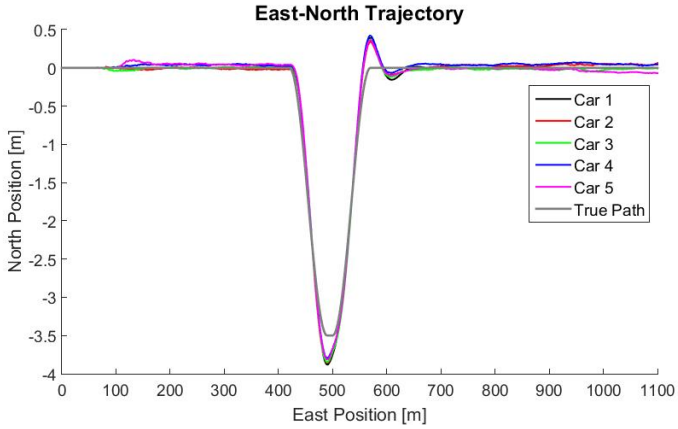

Figure 5.38: East-North Trajectory for Ultimate Lead Following with Autonomous Ultimate Lead

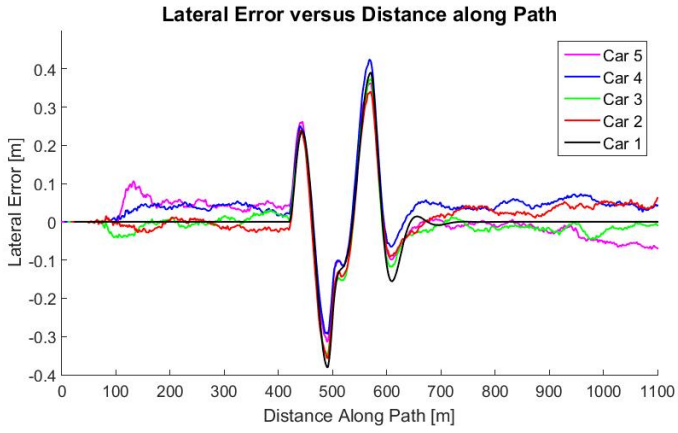

Figure 5.39: Lateral Offset for Ultimate Lead Following with Autonomous Ultimate Lead

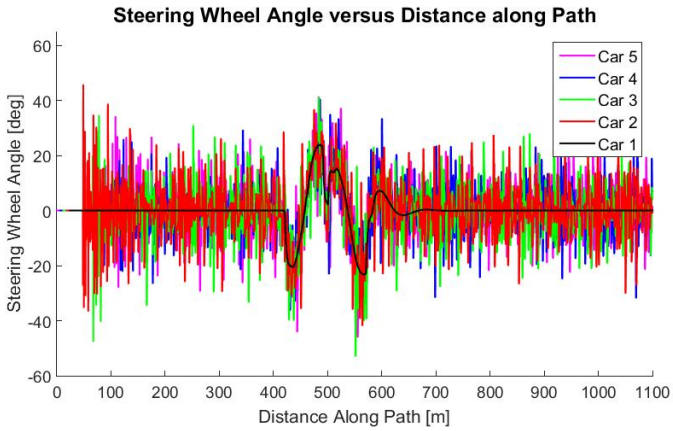

Figure 5.40: Steering Wheel Angle for Ultimate Lead Following with Autonomous Ultimate Lead

Immediate Lead Following

The results are shown in Figures 5.41-5.43. As can be seen, the vehicle's remain stable and exhibit very similar behavior. Once again, with knowledge of the ultimate lead vehicle's lateral offset and heading offset, the maximum lateral offsets of the following vehicle's are halved.

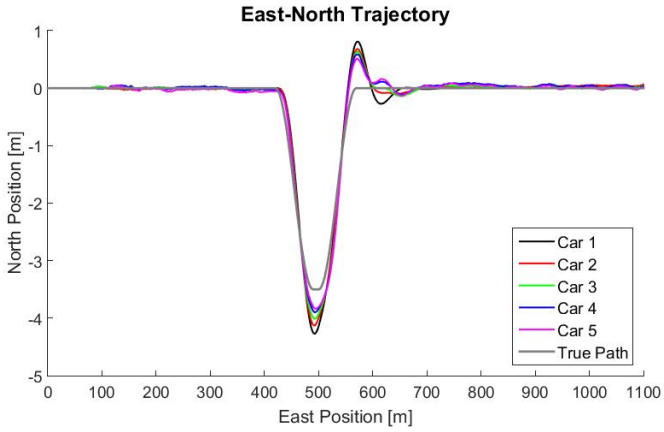

Figure 5.41: East-North Trajectory for Immediate Lead Following with Autonomous Ultimate Lead

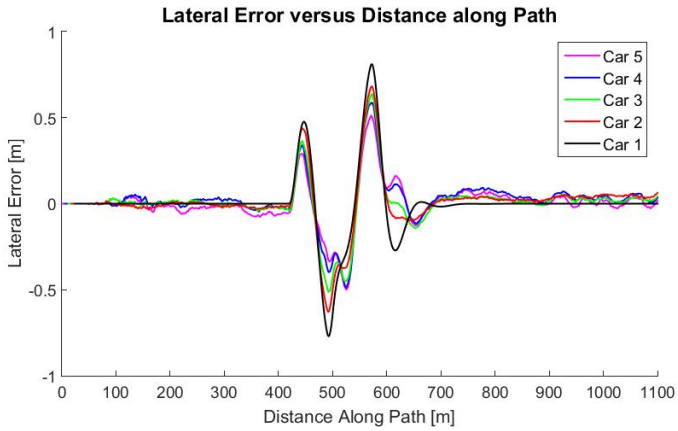

Figure 5.42: Lateral Offset for Immediate Lead Following with Autonomous Ultimate Lead

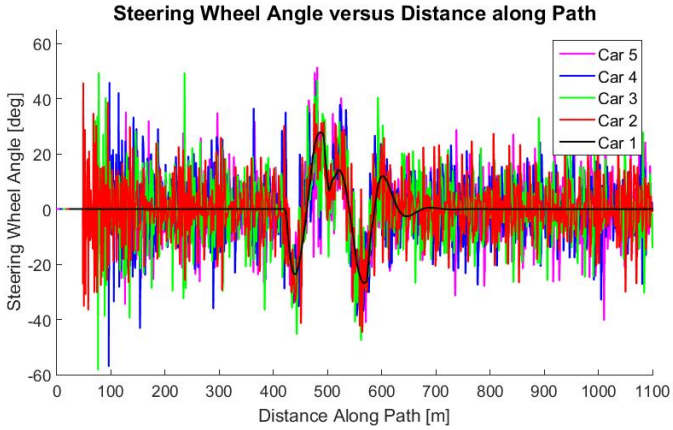

Figure 5.43: Steering Wheel Angle for Immediate Lead Following with Autonomous Ultimate Lead

5.5.3 NCAT Test Track - Banked

Ultimate Lead Following

As in the manually driven ultimate lead case, the following vehicles are able to track the ultimate lead's trajectory. And with maximum lateral errors less than 1 m.

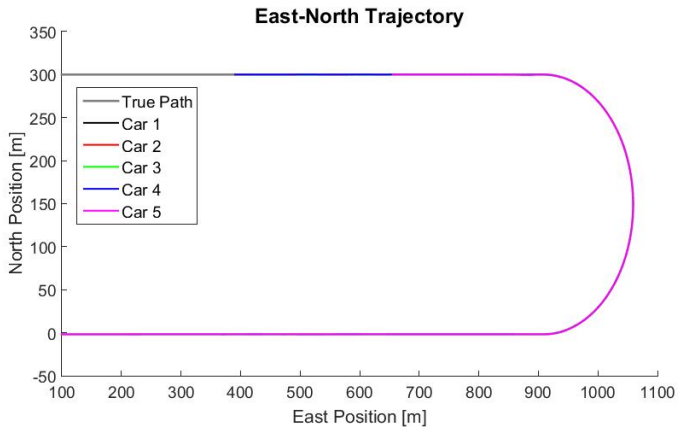

Figure 5.44: East-North Trajectory for Ultimate Lead Following with Autonomous Ultimate Lead

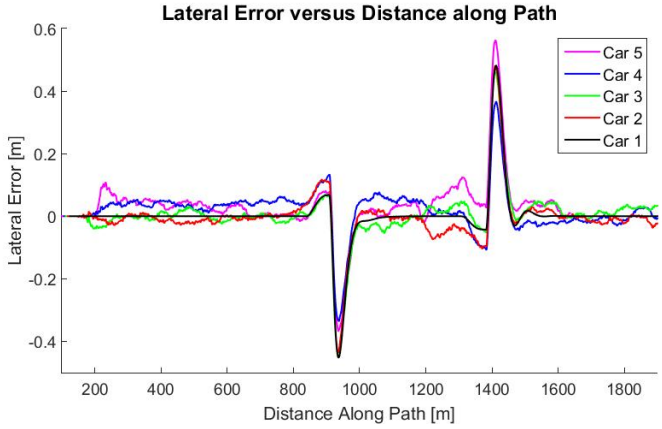

Figure 5.45: Lateral Offset for Ultimate Lead Following with Autonomous Ultimate Lead

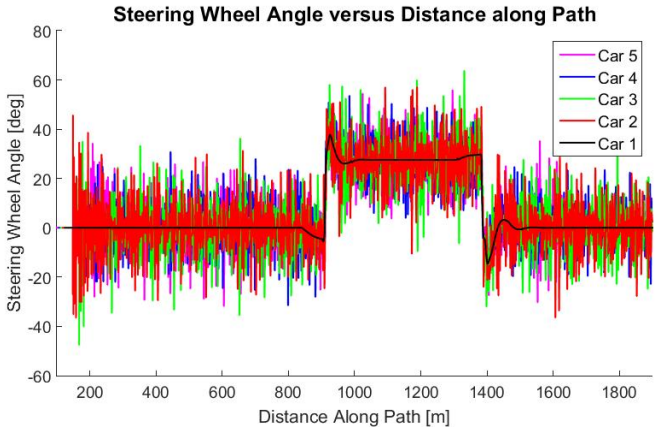

Figure 5.46: Steering Wheel Angle for Ultimate Lead Following with Autonomous Ultimate Lead

Immediate Lead Following

In the immediate lead following case, the maximum lateral errors are less than 0.5 m. Which are less than half the of the lateral errors in the manually driven ultimate lead case.

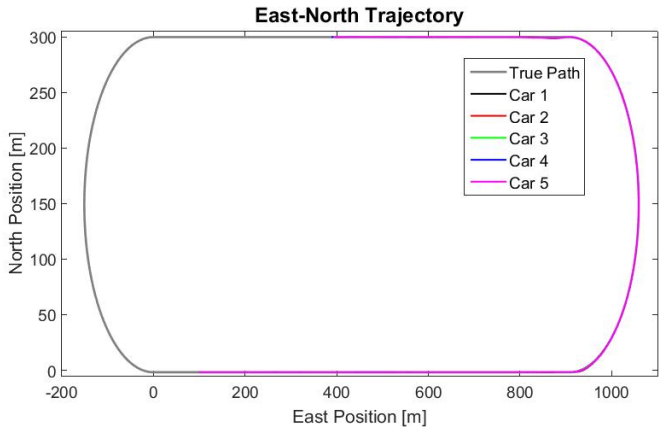

Figure 5.47: East-North Trajectory for Immediate Lead Following with Autonomous Ultimate Lead

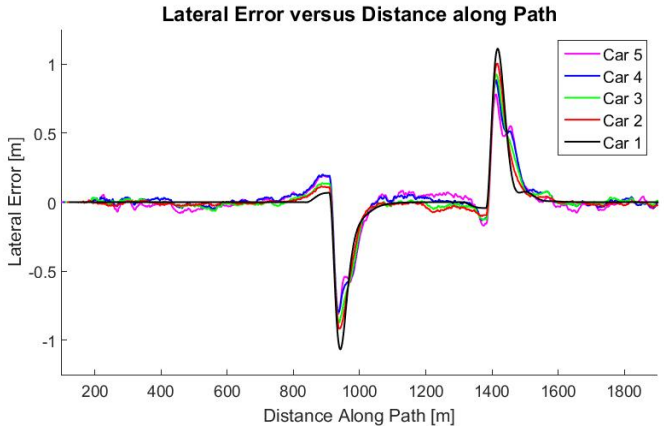

Figure 5.48: Lateral Offset for Immediate Lead Following with Autonomous Ultimate Lead

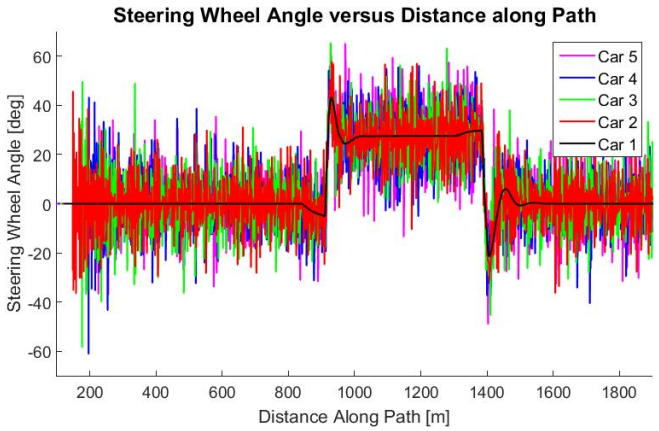

Figure 5.49: Steering Wheel Angle for Immediate Lead Following with Autonomous Ultimate Lead

5.5.4 Immediate Lead versus Ultimate Lead Evaluation

The lateral offset comparisons with an autonomously driven ultimate lead are shown in Figures 5.50-5.52. The lateral offsets are similar just like in the manually driven ultimate lead case; however, the offsets are smaller. This is one of the benefits of an autonomously driven ultimate lead.

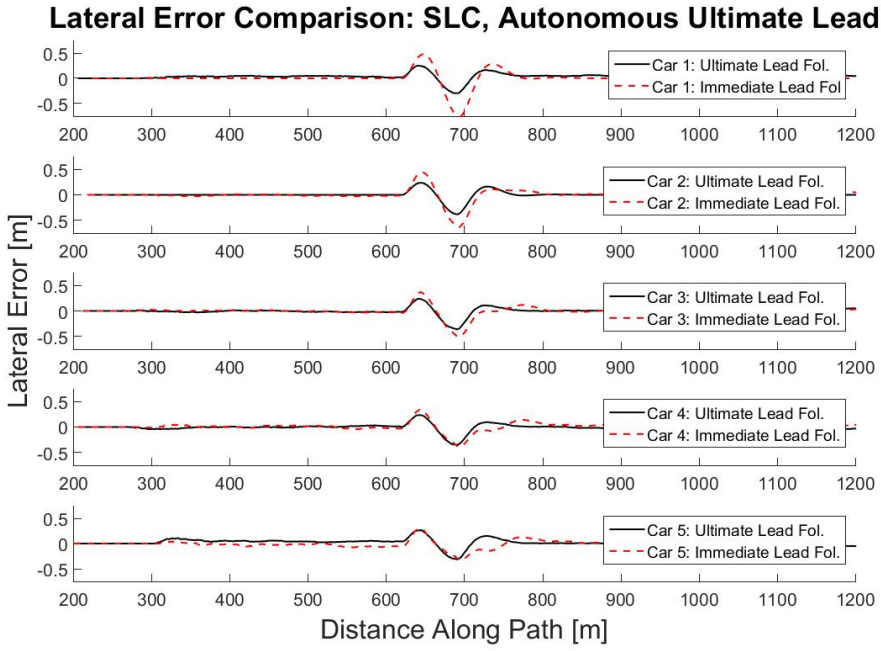

Figure 5.50: Lateral Offset Comparison for Single Lane Change, Autonomously Driven Lead.

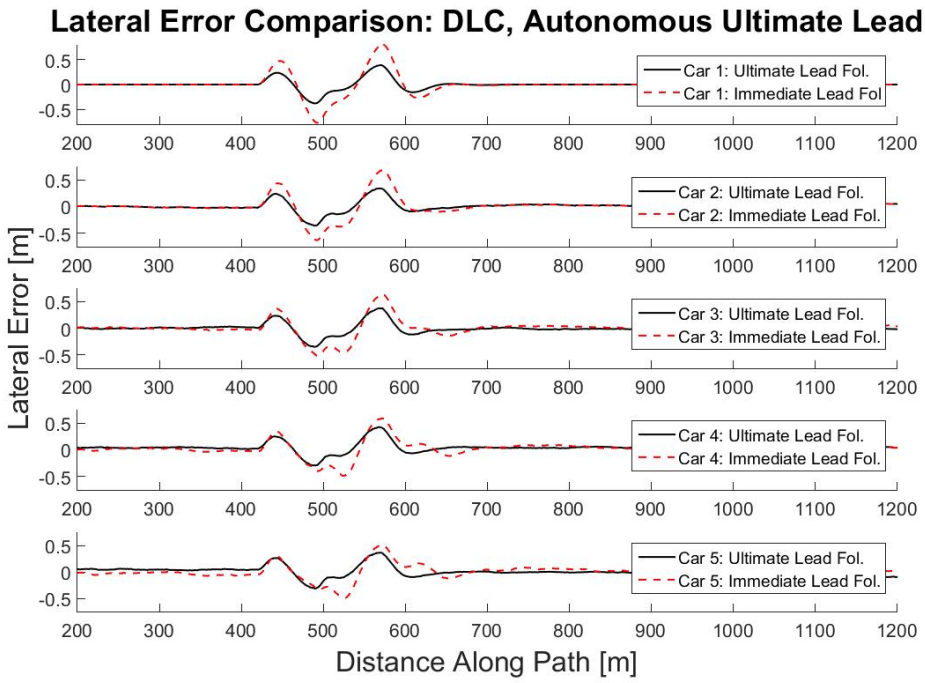

Figure 5.51: Lateral Offset Comparison for Double Lane Change, Autonomously Driven Lead.

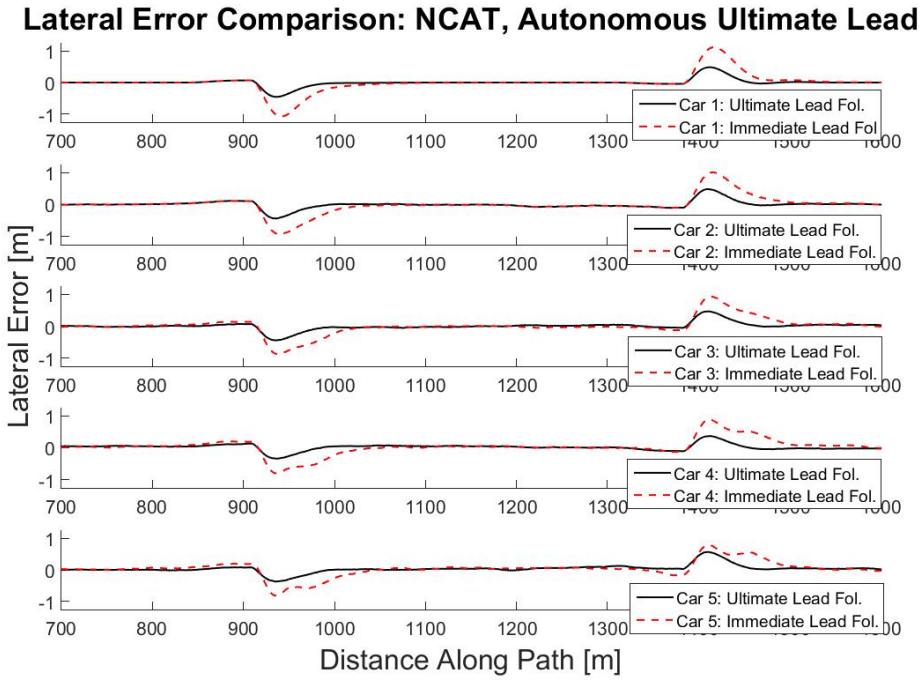

Figure 5.52: Lateral Offset Comparison for Double Lane Change, Autonomously Driven Lead.

5.6 Conclusions

In this Chapter, the layout for the simulation results was given. After which, the simulation environment, CarSim, was described. CarSim's benefits were given as well. Its high-fidelity vehicle models, which have been experimentally verified, are the main benefit of the software. It also outputs all vehicle states and allows users to design custom vehicles. Users may design driving scenarios and perform multiple vehicle simulations too.

The simulation results were presented for a following distance of 325 m. Three different scenario types were evaluated: a single lane change, a double lane change, and travelling around the NCAT test track. Ultimate lead following and immediate lead following was examined with consideration given to both a manually driven ultimate lead and an autonomously driven ultimate lead. The simulations showed that for ultimate lead following and immediate lead following, the convoy exhibits similar lateral offsets. Therefore, both following schemes are feasible; it only depends on the requirements of the environment the convoy is in. The difference between an manually driven ultimate lead and an autonomously driven ultimate lead is that in the autonomously driven ultimate lead case, the maximum lateral offsets are less than half of the maximum lateral offsets of the manually driven ultimate lead case.

Chapter 6

Conclusions and Future Work

6.1 Conclusions

Based around the idea of the string stability of a convoy, this thesis began by presenting some of the most prominent prior works on the subject to give the reader a foundation for the subject. After this, the relative positioning algorithm considered in this work was detailed. A brief description of dynamic base real-time kinematic positioning was examined. The DRTK algorithm takes advantage of the high precision of the carrier phase measurement to calcuate a relative position vector between two moving base receivers. The change in position of the following vehicle may be found using time-differencing of the carrier phase (TDCP) measurement, which also takes advantage of the carrier phase's precision. Using DRTK and TDCP, a reference path was generated based off the lead vehicle's past positions which allowed the lead vehicle to be out of sight. From the reference path, measurements of lateral offset and heading offset with respect to the reference path were determined. These measurements were used as feedback in the control architecture.

With an understanding of how the feedback measurements were calculated, the models used for the development of the lateral and the longitudinal controllers were introduced. The lateral controllers were developed around the lateral, dynamic, bicycle model, and the longitudinal controller was developed based an engine torque model. Also, the two different following strategies were introduced: ultimate lead following and immediate lead following.

For path following control, a classical, cascaded architecture was employed. The inner loop controller was design as a lead compensator. A lead compensator was

then designed for the system. It is desired for the dominant eigenvalue to be real, so that the dominant response is that of a first order decay. For this system, a lead compensator produced a real dominant eigenvalue. A lead compensator was chosen over a PD controller for a couple reasons: a lead controller limits the amplification of high frequency noise, placing the pole at a location other than zero provides less derivative action and more smoothing. Since the main objective of the controller is to have zero lateral error at steady state, a PI controller was implemented for the outer loop. Once the loop controllers were designed, the string stability of multiple vehicles was considered. There were two criterias considered for string stability: the magnitude of the transfer function from lead vehicle's path tangent to the following vehicle's heading error must be less than or equal to one and the impulse response of the lateral offset must be sign-invariant. These were verified for the control scheme presented here when a prefilter was applied to the first following vehicle if the ultimate lead is autonomously driven or to the second following vehicle if the ultimate lead is manually driven.

To test the control scheme in simulation, three tests were performed: a single lane change, a double lane change, and an oval loop scenario. In each scenario, 2 different control schemes were evaluated: ultimate lead following with lead vehicle information and immediate lead following with lead vehicle information. Also, cases where the ultimate lead vehicle is autonomously driven and manually driven were considered. The lateral offsets for each scenario were compared, and it showed that following the immediate lead has an accuracy equal to following the ultimate lead. Therefore, it only depends on which following scheme is more applicable for the convoy's driving scenario.

6.2 Future Work

There are many ways of extending the current work. Firstly, evaluation should be made for the proposed control strategies on Auburn's research vehicle. When testing in a real-life environment, there are issues which are very difficult to predict or model in simulation. Once the control strategies have been implemented on the research vehicles, further examination include a comparison between the proposed GPS following approach versus the camera/radar implementations performed by previous authors. While the GPS approach laid out in this thesis allows the lead vehicle break line of sight, the camera/radar approach is better for urban canyons or other areas with poor satellite geometry.

Another future task would be to pair a camera or LiDAR with the current set up for obstacle avoidance and vehicle safety. For instance, if the ultimate lead vehicle performed a lane change at time t_k, when a following vehicle goes to perform the the same lane change at time t_{k+n}, the lane may no longer be empty or safe to change into. Therefore, a camera, LiDAR, or RADAR could be used to check for obstacles in the way. A path planner could be incorporated into the design to generate an alternate safe route for the follower to take until it is safe to return to the leader's path. Another application of this framework would be in a highway merging situation; where the following vehicle would need to change lanes (or slow down) if a vehicle were merging onto the highway.

Bibliography

[1] W. Travis, S. Martin, D. W. Hodo, and D. M. Bevly, "Non line of sight automated vehicle following using a dynamic base rtk system," *NAVIGATION, Journal of the Institute of Navigation*, vol. 58, no. 3, pp. 241–255, Sep 2010.

[2] S. Darbha, "String stability of interconnected systems: An application to platooning in automated highway systems," Ph.D. dissertation, University of California, Berkeley, 1997.

[3] C.-Y. Liang and H. Peng, "Optimal adaptive cruise control with guaranteed string stability," *Vehicle System Dynamics*, vol. 32, no. 4-5, pp. 313–330, 1999.

[4] J. Ploeg, N. van de Wouw, and H. Nijmeijer, "$\mathcal{L}_p$ string stability of cascaded systems: Application to vehicle platooning," *IEEE Transactions on Control Systems Technology*, vol. 22, no. 2, pp. 786–793, March 2014.

[5] L. Xiao and F. Gao, "Practical string stability of platoon of adaptive cruise control vehicles," *IEEE Transactions on Intelligent Transportation Systems*, vol. 12, no. 4, pp. 1184–1194, Dec 2011.

[6] R. Kianfar, M. Ali, P. Falcone, and J. Fredriksson, "Combined longitudinal and lateral control design for string stable vehicle platooning within a designated lane," in *17th International IEEE Conference on Intelligent Transportation Systems (ITSC)*, Oct 2014, pp. 1003–1008.

[7] S. Solyom, A. Idelchi, and B. B. Salamah, "Lateral control of vehicle platoons," in *2013 IEEE International Conference on Systems, Man, and Cybernetics*, Oct 2013, pp. 4561–4565.

[8] I. Hassanain, "String-stable automated steering in cooperative driving applications," Master's thesis, Delft University of Technology, 2017.

[9] W. L. Jansen, "Lateral path-following control of automated vehicle platoons," Master's thesis, Delft University of Technology, 2016.

[10] R. Kianfar, P. Falcone, and J. Fredriksson, "A distributed model predictive control approach to active steering control of string stable cooperative vehicle platoon," *IFAC Proceedings Volumes*, vol. 46, no. 21, pp. 750 – 755, 2013, 7th IFAC Symposium on Advances in Automotive Control.

[11] O. McAree and S. M. Veres, "Lateral control of vehicle platoons with on-board sensing and inter-vehicle communication," in *2016 European Control Conference (ECC)*, June 2016, pp. 2465–2470.

[12] S. M. Martin, "Closely coupled gps/ins relative positioning for automated vehicle convoys," Master's thesis, Auburn University, 2011.

[13] P. D. Groves, *Principles of GNSS, Inertial, and Multisensor Integrated Navigation Systems*. Artech House, 2013.

[14] W. Travis and D. M. Bevly, "Trajectory duplication using relative position information for automated ground vehicle convoys," May 2008, pp. 1022–1032.

[15] R. Jazar, *Vehicle Dynamics: Theory and Applications*. Springer-Verlag, 2008.

[16] R. Rajamani, *Vehicle Dynamics and Control*. Springer, 2006.

[17] G. F. Franklin, J. D. Powell, and A. Emami-Naeini, *Feedback Control of Dynamic Systems*, 7th ed. Pearson, 2015.

[18] H. Pacejka, *Tyre and vehicle dynamics*, 2nd ed. Elsevier, 2005.

[19] S. Darbha and S. P. Bhattacharyya, "Controller synthesis for sign-invariant impulse response," *IEEE Transactions on Automatic Control*, vol. 47, no. 8, pp. 1346–1351, Aug 2002.

[20] S. Darbha, "On the synthesis of controllers for continuous time lti systems that achieve a non-negative impulse response," *Automatica*, vol. 39, no. 1, pp. 159 – 165, 2003.

[21] W. A. Malik, S. Darbha, and S. P. Bhattacharyya, "On the transient control of linear time invariant systems," in *2009 American Control Conference*, June 2009, pp. 3142–3147.

[22] P. Ioannou and C. Chien, "Autonomous intelligent cruise control," *IEEE Transactions on Vehicular Technology*, vol. 42, no. 4, pp. 657–672, 1993.

[23] M. S. Corporation. (2018) Carsim overview. [Online]. Available: https://www.carsim.com/products/carsim/index.php

[24] P. Misra and P. Enge, *GLOBAL POSITIONING SYSTEM Signals, Measurements, and Performance*. Ganga-Jamuna Press, 2011.

Appendix

A.1 DRTK RPV Calculation

Simply put, the carrier phase is a measurement, in cycles, of the difference between the phase of the carrier signal generated by the receiver and the phase of the carrier signal received by the receiver from the satellite. While this difference of cycles is known with high precision, the number of whole cycles between the receiver and the satellite is unknown. The number of whole cycles is referred to as the integer ambiguity, N. The carrier phase is also corrupted by errors due to the atmosphere, the receiver and satellite clocks, and thermal noise. Combining these into a carrier phase measurement model gives

$$\phi_A^s = \lambda^{-1}[r^s + I_\phi + T_\phi] + \frac{c}{\lambda}(\Delta t_A - \Delta t^s) + N + \epsilon_\phi \tag{A.1}$$

where ϕ_A^s is the carrier phase from satellite s to receiver A, λ is the carrier wavelength, r^s is the true range between the satellite and the receiver, I_ϕ and T_ϕ are atmospheric errors due to the ionosphere and the troposphere, respectively, c is the speed of light, Δt_A is the receiver clock bias, Δt^s is the satellite clock bias, and ϵ_ϕ is the random error due to thermal noise. The method of choice for estimating the change in the integer ambiguity between the two receivers is least-squares ambiguity decorrelation adjustment (LAMBDA), and is laid out in more detail in [24].

With change in the integer ambiguity between the two receivers estimated, the relative position vector may be found using the DRTK algorithm. In DRTK, a single difference is applied between the carrier phase measurements received by the leading vehicle, A, and following vehicle, B, from a single satellite, s. This removes errors

due to the atmosphere and satellite clocks.

$$\Delta\phi^{s}_{AB} = \lambda^{-1}(\Delta r^{s}_{AB}) + \frac{c}{\lambda}(\Delta t_{AB}) + N_{AB} + \epsilon_{\phi_{AB}} \tag{A.2}$$

To remove the errors due to relative receiver clock bias, Δt_{AB}, a double difference is performed. A double difference is the difference of two single differences performed with carrier phase measurements from two satellites, s_1 and s_2.

$$\Delta\phi^{s_1 s_2}_{AB} = \lambda^{-1}(\Delta r^{s_1 s_2}_{AB}) + N^{s_1 s_2}_{AB} + \epsilon^{s_1 s_2}_{\phi_{AB}} \tag{A.3}$$

The double differenced range, $\Delta r^{s_1 s_2}_{AB}$, is related to the relative position by

$$\Delta r^{s_1 s_2}_{AB} = -(\vec{u}^{s_1}_{A} - \vec{u}^{s_2}_{A})\vec{b}_{AB} \tag{A.4}$$

where $\vec{u}^{s_1}_{A}$ and $\vec{u}^{s_2}_{A}$ are the estimated unit vectors between the reference receiver and the satellites, and $\vec{b}_{AB}$ is the relative position vector (RPV) between receivers A and B. The RPV is found by combining Equations (A.3) and (A.4), and performing least squares on the result as shown below.

$$\vec{b}_{AB} = \left[(\vec{u}^{s_1}_{A} - \vec{u}^{s_2}_{A})^{T}(\vec{u}^{s_1}_{A} - \vec{u}^{s_2}_{A})\right]^{-1}(\vec{u}^{s_1}_{A} - \vec{u}^{s_2}_{A})^{T}(\lambda\Delta\phi^{s_1 s_2}_{AB} - \lambda N^{s_1 s_2}_{AB}) \tag{A.5}$$

Note, this assumes the change in the integer ambiguity between the two receivers, $N^{s_1 s_2}_{AB}$, has already been estimated. Also, at this point, the RPV is in the earth-centered, earth-fixed (ECEF) frame and must be transformed into east-north-up (ENU) frame. The DRTK method used is known as dual frequency DRTK; meaning it uses GPS information from both the L_1 and the L_2 frequencies. For more detail on DRTK, see [1]. For more information on dual frequency DRTK, see [12].

A.2 TDCP Odometry Calculation

Equation (A.6) shows the differencing of two instances of Equation (A.1).

$$\begin{aligned}\phi^s_{B_k} - \phi^s_{B_{k-1}} = \lambda^{-1}[r^s_k + I_{\phi_k} + T_{\phi_k}] + \frac{c}{\lambda}(\Delta t_{B_k} - \Delta t^s_k) + N_k + \epsilon_{\phi_k} \\ -\Big(\lambda^{-1}[r^s_{k-1} + I_{\phi_{k-1}} + T_{\phi_{k-1}}] + \frac{c}{\lambda}(\Delta t_{B_{k-1}} - \Delta t^s_{k-1}) + N_{k-1} + \epsilon_{\phi_{k-1}}\Big)\end{aligned} \tag{A.6}$$

Again, when the time between the two measurements is small, the atmospheric errors and the satellite clock errors are nearly constant. Also, if the receiver maintains lock on the carrier phase, the integer ambiguity remains constant. Taking these into account, Equation (A.6) reduces to

$$\phi^s_{B_{k,k-1}} = \lambda^{-1} r^s_{k,k-1} + \frac{c}{\lambda}\Delta t_{B_{k,k-1}} + \epsilon_{\phi_{k,k-1}} \tag{A.7}$$

Replacing the change in satellites to receiver range from sample $k-1$ to k with the ECEF position of the satellites and the ECEF position of the receiver via a relationship similar to Equation (A.4) and assuming the change in the unit vectors from sample $k-1$ to k are negligible, Equation (A.7) becomes

$$\lambda\phi^s_{B_{k,k-1}} - \begin{bmatrix} u^s_{x_k} & u^s_{y_k} & u^s_{z_k} \end{bmatrix} \begin{bmatrix} r^s_{x_{k,k-1}} \\ r^s_{y_{k,k-1}} \\ r^s_{z_{k,k-1}} \end{bmatrix} = \begin{bmatrix} u^s_{B_{x_k}} & u^s_{B_{y_k}} & u^s_{B_{z_k}} & 1 \end{bmatrix} \begin{bmatrix} r^s_{x_{k,k-1}} \\ r^s_{y_{k,k-1}} \\ r^s_{z_{k,k-1}} \\ \Delta t_{B_{k,k-1}} \end{bmatrix} + \epsilon_{\phi_{k,k-1}} \tag{A.8}$$

which can be solved using least squares as in Equation (A.5).

A.3 Derivation of the Bicycle Model

The lateral equations of motion, derived from Figure 3.1, begin with

$$m\dot{V}_y + mV_x\dot{\psi} = F_{yf} + F_{yr} \tag{A.9}$$

$$I_z\ddot{\psi} = aF_{yf} - bF_{yr} \tag{A.10}$$

Assuming small steer angles. Since the tire forces are assumed to remain in the linear portion of the tire curve, the lateral forces become

$$F_{yf} = -C_{\alpha f}\alpha_f \tag{A.11}$$

$$F_{yr} = -C_{\alpha r}\alpha_r \tag{A.12}$$

The slip angles at the front and rear are related to velocities of the wheels.

$$\alpha_f = \frac{V_{yf}}{V_{xf}} - \delta \tag{A.13}$$

$$\alpha_r = \frac{V_{yr}}{V_{xr}} \tag{A.14}$$

where the velocities are derived from the velocity at the center of gravity.

$$V_{xf}\hat{x} + V_{yf}\hat{y} = V_x\hat{x} + V_y\hat{y} + \dot{\psi}\hat{z} \times a\hat{x} \tag{A.15}$$

$$V_{xr}\hat{x} + V_{yr}\hat{y} = V_x\hat{x} + V_y\hat{y} + \dot{\psi}\hat{z} \times -b\hat{x} \tag{A.16}$$

Solving for the corresponding velocities in Equations (A.15) and (A.16), Equations (A.13) and (A.14) become

$$\alpha_f = \frac{a\dot{\psi} + V_y}{V_x} - \delta \tag{A.17}$$

$$\alpha_r = \frac{-b\dot{\psi} + V_y}{V_x} \tag{A.18}$$

From here, simply substitute Equations (A.17) and (A.18) into Equations (A.11) and (A.12), and finally back into the equations of motion to get

$$\dot{V_y} = -\frac{C_{\alpha f} + C_{\alpha r}}{mV_x} V_y + \left[\frac{-aC_{\alpha f} + bC_{\alpha r}}{mV_x} - V_x\right]\dot{\psi} + \frac{C_{\alpha f}}{m}\delta \tag{A.19}$$

$$\ddot{\psi} = -\frac{aC_{\alpha f} - bC_{\alpha r}}{I_z V_x} V_y - \frac{a^2 C_{\alpha f} + b^2 C_{\alpha r}}{I_z V_x}\dot{\psi} + \frac{aC_{\alpha f}}{Iz}\delta \tag{A.20}$$

Note that this is a linearized derivation, assuming small angles.

A.4 Derivation of the Engine Torque Model

There are a few underlying assumptions in the development of the model: the transmission is at steady state (i.e., it is not performing a gear change), the torque converter is locked, and there is negligible longitudinal tire slip. From these assumptions, the wheel speed, ω_w, is directly related to the engine speed, ω_e, by the gear ratio.

$$\omega_w = R\omega_e \tag{A.21}$$

Also, the transmission speed, ω_t, is equal to the engine speed. Following the slip assumption, the longitudinal velocity is

$$V_x \equiv \dot{x} = r_{eff}\omega_w \tag{A.22}$$

where r_{eff} is the effective wheel radius. Differentiating (A.22) gives the longitudinal acceleration

$$\ddot{x} = r_{eff}R\dot{\omega}_e \tag{A.23}$$

The longitudinal equation of motion may be found by summing the forces along the x-axis in Figure 3.1.

$$m\ddot{x} = F_x - R_x - F_{aero} \tag{A.24}$$

where F_x is the sum of the longitudinal forces at all four tires, R_x is the rolling resistance force, and F_{aero} is the aerodynamic drag force. Equation A.23 may be substituted into Equation A.24 and solved for F_x

$$F_x = mRr_{eff}\dot{\omega}_e + R_x + F_{aero} \tag{A.25}$$

F_x is then substituted into the wheel rotation dynamics given by

$$\begin{aligned} I_w\dot{\omega}_w &= T_{wheel} - r_{eff}F_x \\ &= T_{wheel} - mRr_{eff}^2\dot{\omega}_e - r_{eff}R_x - r_{eff}F_{aero} \end{aligned} \tag{A.26}$$

Solving for T_{wheel} gives the torque required to produce a desired acceleration. This may be applied to the transmission dynamics.

$$\begin{aligned} I_t\dot{\omega}_t &= T_t - RT_{wheel} \\ &= T_t - I_wR^2\dot{\omega}_e - mR^2r_{eff}^2\dot{\omega}_e - Rr_{eff}F_{aero} - Rr_{eff}R_x \end{aligned} \tag{A.27}$$

Recalling that $\omega_e = \omega_t$ and the transmission torque is equal to the pump torque (from the steady state transmission assumption), Equation A.27 becomes

$$I_t\dot{\omega}_e = T_p - I_wR^2\dot{\omega}_e - mR^2r_{eff}^2\dot{\omega}_e - Rr_{eff}F_{aero} - Rr_{eff}R_x \tag{A.28}$$

Solving for T_p gives a pump torque load of

$$T_p = \left(I_t + I_wR^2 + mR^2r_{eff}^2\right)\dot{\omega}_e + Rr_{eff}F_{aero} + Rr_{eff}R_x \tag{A.29}$$

which may be substituted into the engine rotational dynamics given by

$$\begin{aligned} I_e\dot{\omega}_e &= T_{net} - T_p \\ &= T_{net} - \big(I_t + I_w R^2 + mR^2 r_{eff}^2\big)\dot{\omega}_e - Rr_{eff}F_{aero} - Rr_{eff}R_x \end{aligned} \tag{A.30}$$

Substituting for the aerodynamic drag force and solving for $\dot{\omega}_e$ results in the first-order ordinary differential equation

$$\dot{\omega}_e = \frac{1}{J_e}\big(T_{net} - c_a R^3 r_{eff}^3 \omega_e^2 - Rr_{eff}R_x\big) \tag{A.31}$$

where

$$J_e = I_e + I_t + R^2 I_w + mR^2 r_{eff}^2 \tag{A.32}$$